Analysis of Seasat-A SAR of the Detection of Oil on the Ocean Surface

Final Report on NOAA Contract ~~NA99SA00734~~ NA79SAC00734

Principle Investigator:
Dr. John E. Estes

Authors:
Michael J. Wilson
Earl Hajic

Geography Remote Sensing Unit

October 6, 1980

TABLE OF CONTENTS

Analysis of Seasat-A SAR Data
for the Detection of Oil on the Ocean Surface

ABSTRACT

In evaluating the capability of the Seasat-A Synthetic Aperture Radar to detect the smoothing effects of oil slicks on ocean surfaces, two problems were encountered. These were: 1) lack of of concurrent surface verification data, and 2) the appearance of so called confusion targets in the imagery. To "synthesize" necessary surface truth information, a linear deterministic oil trajectory model has been developed which sums the effects of winds, currents, and tides to predict hourly oil slick configurations within the Santa Barbara Channel study area.

Using output oil slick trajectory predictions as a guide, a collection of 128 X 128 byte subimages was gathered from oil affected areas. Zones of reduced backscatter which could not be attributed to oil/surface tension effects (confusion targets) provided a similar set of subimages. Taking the two-dimensional Fourier transforms of these subimages and filtering via eight concentric ring masks allowed comparison of normalized mean power distribution as a function of spatial frequency. These comparisons show a more rapid drop off in normalized power at higher frequency for oil slick images than for non-oil slick images. The optimum discriminant, of those tested, utilized the sum of normalized power from the six ring filters representing highest spatial frequency. Separation in this case was achieved at a 99 % confidence level.

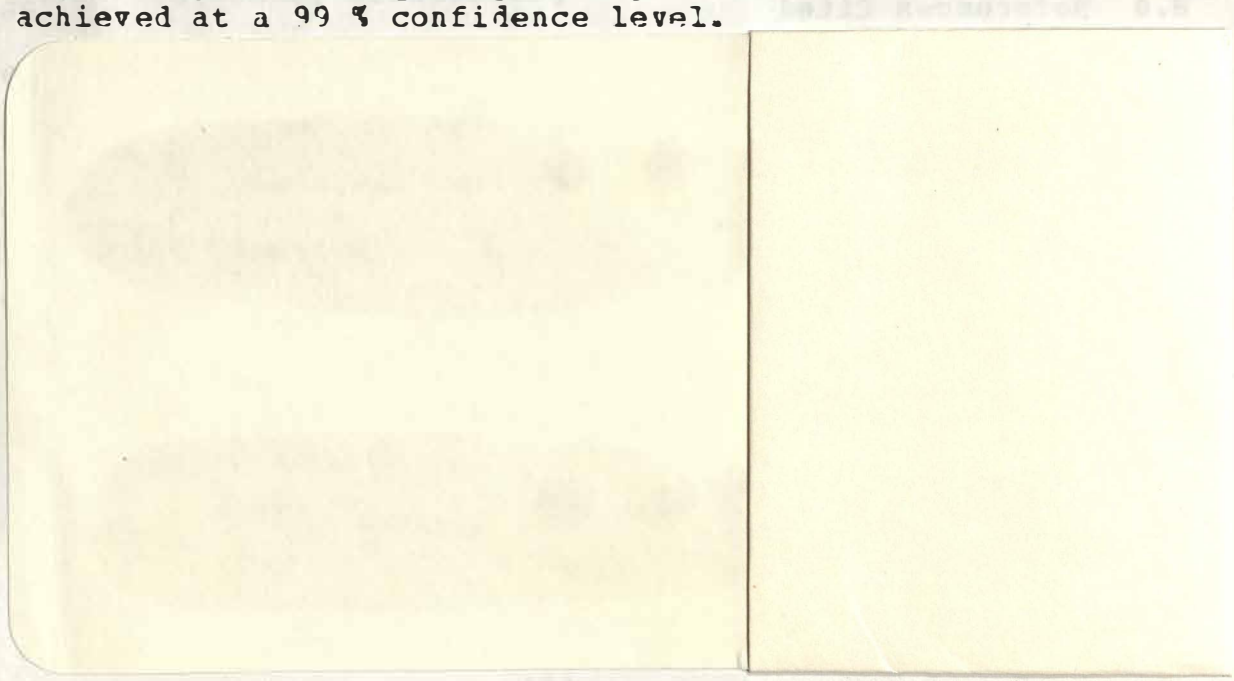

1.0 Summary

A number of oil detection studies employing side looking radars have been conducted in the Santa Barbara Channel capitalizing on the perennial natural seepage which occurs in the area (Kraus et al., 1977) (Kotlarski and Anderson, 1977) (Mauer and Edgerton, 1975). These studies have involved aircraft flown systems utilizing both real and synthetic aperture. Methodology has uniformly focused on the comparison of radar imagery with simultaneously acquired surface verification data consisting primarily of low altitude aerial photography. This technique provides a useful means of gauging actual detection success ratios.

As originally proposed, the research described herein was to use this same sort of comparison technique to test the ability of the Seasat-A Synthetic Aperture Radar (SAR) to detect marine oil slicks from its 800 km orbiting altitude. The study area was again to be the zone of most prolific natural seepage which occurs offshore between the City of Santa Barbara and the University of California some 12 miles to the west (see fig 1.1). Unfortunately, the premature failure of the satellite's electrical system on October 10, 1978 came before any experiment was scheduled; hence no concurrent surface verification data was gathered.

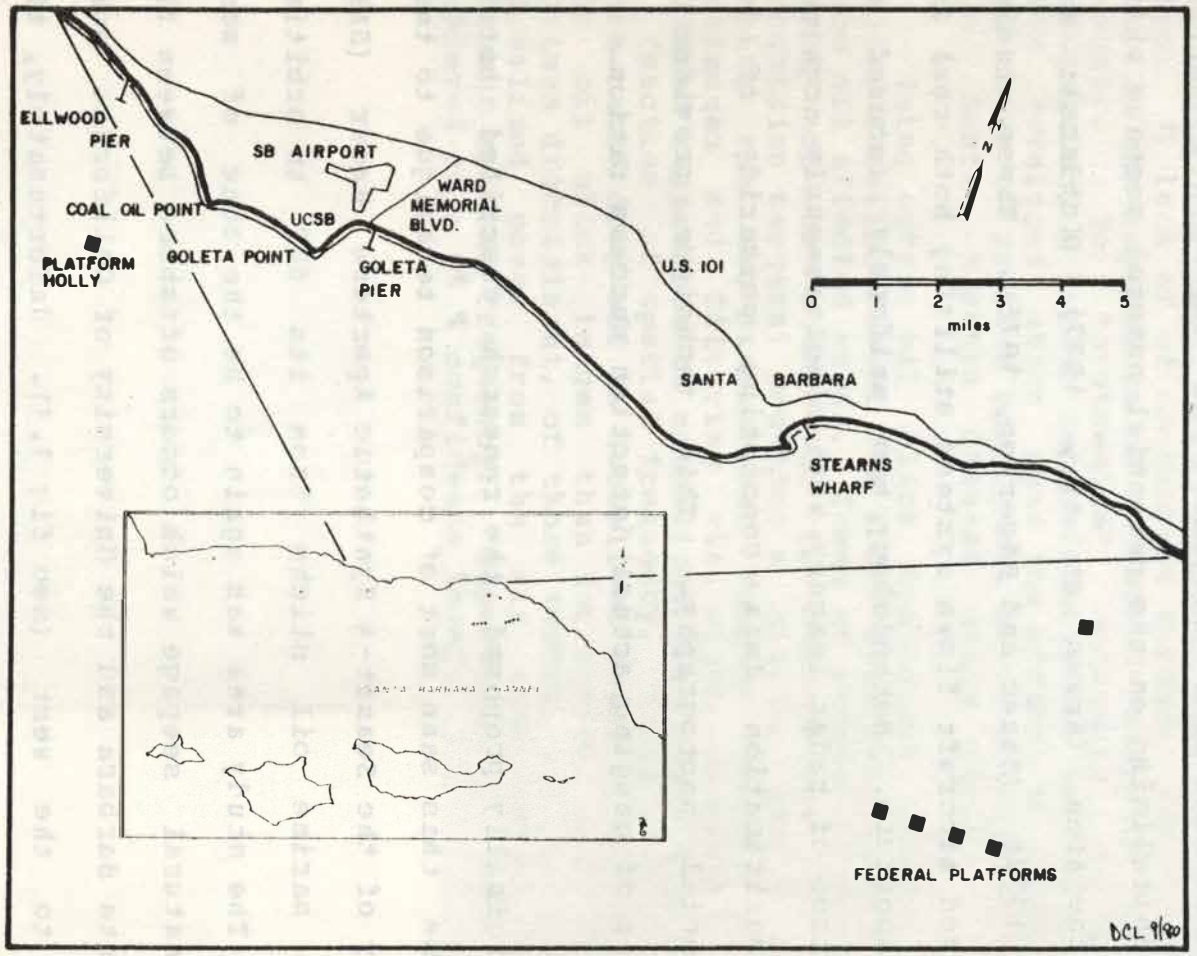

Fig. 1.1 shows the study area and its relative orientation with respect to the rest of the Santa Barbara Channel. Prime natural oil seepage zones occur from the Federal Platforms to Coal Oil Point.

In subsequent evaluation concerning the feasibility of salvaging any portion of the research project it was established that three Seasat SAR imaging overpasses of the Santa Barbara Channel had been completed. These were revolutions (Revs) 308, 552, and 617 which occurred on July 18, Aug 4, and Aug 8, 1978 respectively. Given this information and the predictable nature of oil seepage in the study area a descision was made to pursue the project. Accordingly, new techniques were developed wherein oil slick configurations and positions for the three overpass days were calculated based on known points of origin and the combined influence of wind, current, and tide. Using such "synthetic surface truth" data for comparison, the indication is that the Seasat SAR did successfully detect surface oil slicks in the Santa Barbara Channel. Zones of reduced backscatter (up to 6 dB reductions) occur in the SAR imagery in positions and orientations which closely resemble predicted oil coverage.

A significant problem of confusion targets has also been encountered however, in that several areas which cannot be associated with surface oil slicks exhibit the same reduced backscatter on the imagery. An effort to separate these targets of similar appearance has been made which utilizes spatial frequency (Fourier) transforms of the features in question. The assumption has been that the

amplitude reducing effect of oil on ocean surface waves is frequency specific and hence might produce a characteristic signature on such transforms. Subsequent frequency filtering of these transforms has produced a discriminant which separates the two target types on a cumulative basis at a 99% significance level.

As the ocean surface wave frequencies at which the amplitude dampening forces of oil operate are well above those detected on the transforms, the exact mechanism causing this result is unknown. What is apparent, however, is that normalized power drops off more severely with increasing spatial frequency for bona fide oil slick images than for similar appearing, reduced backscatter, non-oil images.

In describing these results, the following report deals, by necessity, with a diverse selection of topics in image interpretation, flow dynamics, and microwave remote sensing. An attempt has therefore been made to provide pertinent introductory information in each sub-category of investigation. The first such deals with the interaction of imaging radar and ocean surface roughness as altered by oil slicks.

List Of Symbols

W_r	-	radar backscatter power from a point target
W_t	-	transmitted power
G_t	-	gain of the transmitting antenna
A_r	-	effective aperture of the receiving antenna
σ	-	the backscattering cross section of the target
R	-	slant range from radar to target
τ	-	pulse length in seconds
λ	-	radar system wavelength
φ	-	incidence angle
h	-	height above a smooth datum
β	-	depression angle (90 - φ)
L	-	antenna length
c	-	speed of light 3 X 10^{10} cm/sec

Imaging Radar and Oil Slicks

2.1 Imaging Radar Geometry

Imaging radars are active sensors which use the speed of light in one dimension and sensor velocity in the other to define an image plane. An image is created (in the range dimension) by the variable return of incident electro-magnetic radiation (EMR) from points along individual scan lines. These scan lines are not formed by any mechanical motion of the radar antenna. Rather they occur as a by product of an oblique look angle - hence the name side looking airborne radar (SLAR). Radar pulses propagate outward at the speed of light. As they encounter variably reflective surfaces they are returned or backscattered towards the radar. Their arrival back at the receiver is expanded into a brief time series where separation in time represents separation in distance. This time series is one scan line which defines the so called range or cross track dimension of the image. The along track or azimuth dimension is provided for by the incremental advance of the sensor platform from one pulse to the next.

2.2 The Radar Equation

The portion of an incident radar pulse that is returned to the sensor is called the backscatter cross section coefficient (σ). In this context σ represents the reflective characteristics of a point target. The radar backscatter power (W_r) from the same point target is

$$W_r = \frac{W_t \, G_t \, A_r \, \sigma}{(4\pi R^2)^2}$$ (Skolnik, 1970).

A three dimensional surface target, however, is generally considered as a collection of point targets which contribute independent returns of random phase. The average of these returns from a complex scattering surface is

$$\bar{W}_r = \int \frac{W_t \, G_t \, A_r \, \sigma_o \, da}{(4\pi R^2)^2}$$ (Moore and Fung, 1979).

Here σ_o signifies a differential backscatter coefficient or backscatter per unit area. The integration is carried out over the area contributing to the return at any moment. Due to the monochromatic nature of the signal and the random phase of returns, however, the instantaneous power received from any given target will fluctuate widely.

For sensor power the fluctuations are approximated by an exponential distribution or for voltage by a Rayleigh distribution (Moore and Fung, 1979).

The backscatter cross section coefficient then is a continuous measure of the physical and electro-chemical state of the target. The chemical and electrical properties of a surface participate in determining the degree to which incident microwave EMR will be absorbed, transmitted, or reflected. The two properties can be adequately described with one complex number - the complex dielectric constant. This constant is uniformly high over the ocean surface providing virtually complete reflection within the 0.1 to 100 centimeter microwave spectrum (Long, 1975). Since little variability in σ is attributable to deviation in dielectrics for SLAR imagery of an ocean surface, this parameter will be ignored.

2.3 Surface Roughness and Backscatter

Morphology is thus the primary factor controlling radar backscatter from an ocean surface. For a perfectly smooth surface all incident radiation is specularly reflected forward and nothing returns to the receiver. At some threshold roughness level, scattering tends away from purely specular towards a diffuse mode and some incident EMR is

directed back at the sensor. This level of surface height variability is called the Rayleigh roughness length and is dependent on the specifices of radar wavelength and look angle. The relationship is $\lambda/8 \sin \beta$ (Sabins, 1978). Roughness length for an ocean surface is closely linked to surface stress, which is a function of wind speed, current velocity and direction, and the air/sea temperature gradient (Weissman and Thompson, 1977). Increasing surface stress produces more reflective facets on the sea surface which are normal to the impinging microwave beam and hence a higher received backscatter signal at the sensor.

There is an additional consideration which must be made in developing the backscattering criteria for an ocean surface. As wave fields are periodic perturbations the opportunity exists for phase reinforced multiple reflections. This reinforced reflection effect has been termed Bragg scattering. It is both wavelength and depression angle dependent with the critical surface wave length being determined by

$$\text{Bragg } \lambda = \lambda \, 2\cos \beta \quad \text{(Raney and Lowry, 1978)}$$

It is the general consensus that modulation of these critical capillary waves onto lower frequency swell slopes accounts for much of the variability observed in SAR

imagery. The Bragg wavelength for Seasat-A SAR system and geometry is approximately 33.6 cm.

2.4 The Oil Slick Signature

Oil on the ocean surface alters the distribution of water wave frequency components and reduces their amplitudes. It depresses capillary and ultra gravity waves by increasing surface tension, which is the restoring force for these short period waves. It additionally interferes with the wind's ability to create longer period gravity waves (Barger and Garett, 1970). The predictable response of imaging radar to this reduction in surface roughness is a decreased return for areas within the oil slick. This response has been documented in a number of independent studies on both aircraft imagery of ocean oil slicks (Guinard and Purves, 1970) (Mauer and Edgerton, 1975) (Kotlarski and Anderson, 1977) and fixed mount imagery of small slicks in a controlled environment (vanKuilenburg, 1975) (Krishen, 1972). In the latter instance 5 to 10 db reductions in sea surface backscatter (σ_{sea}) have been reported for 13.3 GHz vertically polarized radar imagerys obtained over depression angles ranging between 40° - 75° (Krishen, 1972). This result should be regarded as something of a "best case" however as many factors militate to reduce such a high contrast ratio.

Previous work then seems to imply that given a single frequency sensor with a set viewing angle, the ocean surface should specularly scatter incident microwave EMR away from the receiving antenna until some threshold capillary wave frequency and/or roughness amplitude appears in the wave spectrum. With these threshold conditions met a relative increase in backscatter would be evident on the image. By contrast it is the mechanical reduction of such surface roughness which causes marine oil slicks to be detected by imaging radars. Limiting conditions on such detection then involve both background ocean backscatter (σ_{sea}) and the SAR system noise level. These relationships are discussed in greater detail in the following section.

The Seasat-A Synthetic Aperture Radar (SAR)

3.1e Data Acquisition and Reduction

The Seasat A SAR system used a pulsed transmitter, an antenna and a phase coherent receiver. A short pulse was transmitted toward the surface viaea 2.16 m wide by 10.74 m long antenna. This provided coverage of a 6.2° elevatione plane with the antenna boresight oriented at 20° from nadire and 90e from the Seasat velocity vector. Thusea range swath width of 100 km offset 290 km to the right of the sub-satellite track was achieved from the 800 km high orbit.

Range resolution was determined by the effective pulse length. Specifically, high range resolution was obtained via wide bandwidth pulses and phase coherent reception and processing. The Seasat SAR used a linear frequency change within a 33.4 μsec period at a carrier frequency cf 1274 MHz and a pulse repetition frequency of 1645 pulses per second. This frequency modulated (FM) pulse prcvided for a pulse compression ratio of 634 to 1 on received-signal processing. The result was a range resolution of:

$$\frac{c\tau}{2} \times \frac{1}{634} = \frac{3 \times 10^{8} \text{ m/sec} \times 33.4 \times 10^{-6} \text{ sec}}{1268} = 7.9 \text{ m}$$

Subsequent registration and signal averaging of 4 such range-resolved images resulted in the finad 25 m range resolution and a less noisy (speckled) image (Jordan, 1978).

In the azimuth (along-track) direction, high resolution is also a result of the coherency of the SAR. Since the antenna coverage in the azimuth plane is 15 km, an extensive azimuth-coherent phase history of each "elemental' target was received (some 3000 related returns). The echos were mixed with the coherent local oscillator to provide this hisory. The echos were translated to S band and sent via data link to be recorded on both film and magnetic tape and later coherently processed to generate each azimuth resolution element. This correlation procedure has been discussed in great detail for both optical (Shuchman, et al., 1978) and digital (Wu, 1980) modes, and hence will not be discribed herein.

During the generation of the synthetic aperture in azimuth, each resolution element 'experienced' an effect termed range migration due to the fact that the antenna was not pointed in a direction exactly normal to the velocity of the spacecraft relative to the imaged elements. This effect caused range displacement of up to 72 range- resolution elements. Spectral analysis of the returned signal was used

to determine this effect and compensate for it.

There are two aspects in which the SAR system is extremely fragile. The first centers around the phase coherence requirement for accurately recording the Doppler spectrum. In order to provide the necessary accuracy absolute stability in the real aperture to within $1/4\lambda$ (Beal, 1979) is required. This requirement applies as well to the long synthetic aperture though not in an absolute sense. Platform positional information can be used to calibrate out flight path aberrations creating adequate relative accuracy. Secondly, the Doppler shift of the radar return is dependent on the relative velocity of the target with respect to the sensor. The assumption that a specific target is stationary is a requirement for unambiquous spatial positioning. Targets in motion in the image plane impart an additional frequency shift to their backscattered return which in some cases causes them to be mislocated and in other cases to not be detected at all (Raney and Lowry, 1978).

This latter concern raises questions as to the imaging capabilities of the Seasat SAR system with respect to ocean surfaces which are in constant motion. This motion is subdivided into group, phase, and orbital velocity components, any one of which could dominate modulation of

backscattered radar signal. The uncalibrated/unreferenced Doppler shift that results from a target with such independent velocity components will result in spatial ambiguities involving both swell angle and position (Raney and Lowry, 1978).

3.2 Some Considerations on Radar Imaging of Oil Slick / Ocean Patterns

There are some basic and more specific considerations of the oil slick detection and identification process that supply a useful context for our SAR analysis. These generally involve variations in effective values of sea backscatter cross section under normal (σ_{sea}) and oil slick (σ_{slick}) conditions.

1.a Slick spectral character - The contrast ratio (σ_{slick} +a N)/(σ_{sea} + N) must initially be sufficient to enable ana oil pattern to be discerned from a water background in SAR imagery. Once this 'just noticeable' threshold is detected there are grounds for examining the difference in the energy spectral distributions of the imaged oil slick vs. the imaged non-slick background. One would expect that the oil slick regions would show decreased high frequency components as the mechanical damping effect is concentrated in the capillary and ultragravity surface wave region (see fig.

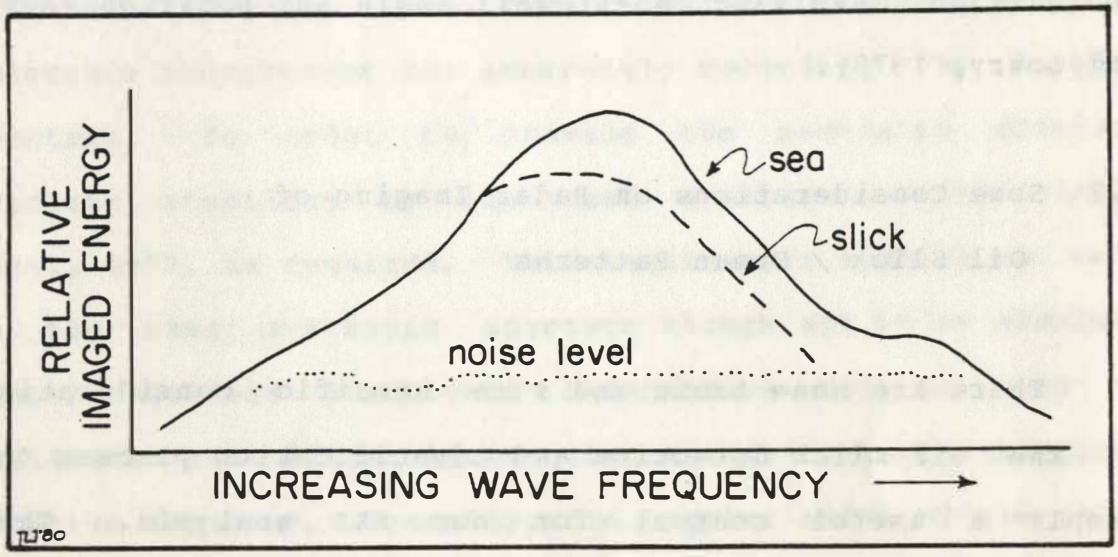

Fig. 3.1 is an idealized representation of reduced high frequency backscatter energy (wave damping) due to marine surface oil slicks.

3.1). As an analogy, Schuchman, Kasischke, and Klooster (1978) noted that for both the optically and the digitally generated spectra many more high frequency components were present in the Gulf Stream spectra than in the spectra of the non-Gulf area. A limiting condition on the spectral differences, however may occur when σ_{slick} approaches the SAR noise level and its relatively white, uniform spectral distribution. Mitsuyasu (1978), with data for a wind speed of 8 m/sec, confirmed earlier studies of Pierson and Stacy (1973) which describe the spectral density form in the gravity-capillary range. This form is almost independent of the fetch and is unaffected by the existence of the large dominant waves in the gravity range. Mitsuyasu divided the high frequency part of the wind-wave spectrum into two typical regions: The gravity equilibrium range of $f_m < f <$ 4 Hz (where f_m is the spectral peak frequency, < 1 Hz), and the gravity-capillary range 6 Hz < f < f_u (where the upper frequency limit, f_u, is at least 14Hz). The range 4-6 Hz is considered as a transition range. The spectral energy decreases proportional to f^{-5} in the gravity equilibrium range and proportional to f^{-4} in the gravity-capillary range and is wind speed dependent.

Wright (1968) summarized pertinent conclusions of Cox and Munk (1954) about sea surface slope statistics (from sun glitter measurements) and found that the mean-squared slope

in the presence of slicks was about 1/3 that in the absence of slicks. Water waves of 30 cm wavelength were damped by a factor of 100.

2.0 Boundary effects - There is presently insufficient information on the nature of $\sigma_{slick} / \sigma_{sea}$ at the pattern boundaries to base slick identification on images of boundary conditions, however some work in this area has been completed. Pilon and Purves (1973) noted that at 35 cm Bragg wavelengths (428 MHz radar) the slick to sea scattering cross section boundary was such that scattering was still significant within the slick, decaying about 150 m of the 'edge'. In contrast, decay was about 1/10 that distance (17 m) for 12 cm Bragg scattering (1228 MHz radar) imagery. These observations were for vertically polarized, grazing incidence waves and a synthetic aperture.

3. Pattern recognition and confusion targets - The next level of concern is that of oil slick pattern recognition/identification in an environment of possible similar patterns. Here a priori information of suspect oil slick/spill regions, natural seeps, relatively unique slick configurations and/or corroborating information from other sensors, ships, oil platforms, etc., is important. For a region of natural seepage such as the Santa Barbara Channel, the possibility of obtaining radar imagery of characteristic

and identifiable slick configurations is certainly real. Kraus et al. (1977) have provided a quantitative and comparative summary of the detection performance of a real and a synthetic aperture side-looking radar (AN APS-94D and COR). These X band radars had H and V polarization respectively. Detection probabilities of the known surface slicks (natural oil seeps and oleyl alcohol spills) were .29 and .66 on one date (winds 220° T at 10 kt, 3 foot swells at 270° T). Our concern here, however, intentionally places more stress on evaluating the Seasat-A SAR as a major oil slick identification sensor. Thus, windrow effects on the Channel surface caused by vorticity in surface wind and/or current fields can be a significant source of pattern noise, as can areas of zero surface stress.

4. Noise in the contrast ratio - The fact that an oil slick pattern is established on radar imagery by the relative lack of sea backscatter can be a significant problem in itself. Emphasized in the context of relatively low-level sea backscatter conditions which prevail in the Santa Barbara Channel, maximum pattern contrast is asymptotically limited by receiver and/or system noise considerations. At relatively low sea states (and, hence, relatevely low σ_{sea} levels) receiver noise may be a significant fraction of the σ_{sea} + noise output, in which case the σ_{sea} / N ratio will be relatively small. Since the

slick is forcing (at best) σ_{sea} to zero, the contrast ratio in the limit becomes $N / (\sigma_{sea} + N)$.

5. Ocean surface backscatter models - Most of the abundant speculation which accompanies the interpretation of ocean SAR data arises from the lack of a uniformly accepted description of the functioning imaging mechanism. The problem is complex, and made more so by the nearly random returns associated with the destructive and constructive interference which results from a monochromatic illumination source. Several models for radar imaging of ocean surface waves have been developed however, and these have been summarized by Elachi and Brown (1977). They are termed the

oa tilt modulationa
oa roughness modulationa
oa orbital velocity anda
oa parametric effects

models. These models describe ocean wave periodic modulation of the imaged sea backscattering elements (e.g., the capillary waves). Each model gives a different modulation ratio of σ_{sea} depending on the angle between the flight line and the wave and wind directions. Though their interest is primarily the contrast ratio of the ocean wave pattern of wavelengths $\sim$2x SAR resolution, their study of the factors contributing to σ_{sea} within an azimuth-range resolution cell is pertinent. Some sea states which produce

significant variation of wave tilt or orbital velocity may be beyond the region to be evaluated. For example, in the orbital velocity roughness model, small waves are strained by the horizontal component of the orbital motion of larger waves. This results in the ripples being shortened and steepened on the forward face of a larger wave and spread out and flattened on the backward face. This leads to modulation of the surface roughness by the large wave (Elachi and Brown, 1977). Whether (and where) the orbital velocity horizontal component strains the oil film beyond the tension limit is an important consideration in defining the nature of the $\sigma_{slick} / \sigma_{sea}$ contrast ratio curve. Raney and Lowry (1978) examined the models of Elachi and Brown (1977) to show that long swells modulated by capillaries could be represented by an imaging model based on the orbital motion of the capillaries along with the vertical component of the underlying gravity wave motion. This sea roughness model can represent conditions in the Santa Barbara Channel and would be suitable as a background (σ_{sea}) condition for a contrasting slick -- assuming significant reduction of capillary waves.

3.3 Irregularities in the Seasat-A SAR Data and the Impact of Performance Variationsr

Seasat SAR performance variations have been reported

that can affect image quality and oil slick detection/identification to varying degrees. These variations are here summarized and their impact on oil slick detection estimated.

1. Sensitivity time constant - STC compensates for known variations in antenna gain vs. angle in the range direction. A linear decrease in receiver gain of 9 db from near to mid-range is followed by a similar gain increase from mid to far-range. A mispositioning of the gain algorithm of 45-55 μsec, as reported, is equivalent to a range vs. gain mispositioning of 7.5 km, with a 9 db/50 km gain slope. This could have resulted in up to a 1.35 db incorrect gain setting. Data processing compensations, however, have removed all but some 1 db variation about the preferred function. The remaining effect is a slight decay in density for constant backscatter at increasing range.

The impact of this factor to SAR oil detection capabilities is marginal under relatively high contrast ratios of $\sigma_{slick} / \sigma_{sea}$, but can be significant where this contrast between oil and the ocean surface may have been only -2db to -3 db, or at a high gain condition, where receiver saturation level is below the return of normal sea clutter (see fig 3.2).

2. Aspect Ratio - Inconsistencies from the desired unity aspect ratios have been reported for some processed imagery. Range/azimuth ratios of 1.17, 1.08, 1.01, and, .94 were noted in 4 swaths (SAR Panel: GOASEX, April 1979). Such variation does not affect the $\sigma_{slick} / \sigma_{sea}$ ratio and has little to no significant effect on oil slick pattern recognition per se. Oil configurations are but loosely defined and variants due to winds, tides, currents, tempefature, etc. create pattern uncertainties far in excess of these aspect ratio deformations.

3. Cross track - Slant to ground range gecmetric rectifications contain errors of about 3%. The impact of such errors is similar to but less than the considerations of #2 above.

4. Temperature related gain change - Temperature changes caused a 1/2 db gain variation in the SAR sensor. This change has essentially no (or very small) impact on the $\sigma_{slick} / \sigma_{sea}$ ratio, except for very low ratios near 0 to -1 db at the highest gain settings. This variation in gain can act as an additive deleterious effect to other performance variations.

5.e Signal leakage related gain change - Signal leakagee has reportedly caused a 1 to 10 db uncompensated gain

change. This can have a significant worsening impact on $\sigma_{slick} / \sigma_{sea}$ ratios. The net effect is to drop the average sea model signal level closer to the system noise level. Figs. 3.2, 3.3, and 3.4 (Jordan and Rodgers, 1976) (Jordan,a 1978) show this progressive contrast reduction from high thru nominal to low gain mode. If the maximum oil slick effect is a total masking of the average sea model return, then the 'best' the slick can do is reduce the return to the thermal or system noise level. Thus, at nominal gain, a $\sigma_{slick} / \sigma_{sea}$ contrast ratio of -10 db is reduced to -6 db (at the mid-range of the image, ie 290 km from nadir). This type of change occurs when there is relatively low initial and hence only nominal initial receiver gain decreased to low gain by the effects of signal leakage.

More optimistically (and less likely), the change due to signal leakage may be similar to the change from high to nominal gain (a 9 db change): here the $\sigma_{slick} / \sigma_{sea}$ contrast will change from -11 db to -10 db. Note however, that these are optimum ratios, whereas, most likely an oil slick will not reduce the backscatter from the slick-image area to the receiver noise or system noise level. Depending on wind, sea state, and other factors, the σ_{slick} / noise ratio will be variable and generally > 1 (or 0 dB).

6. Linear feature offset - Due to a change in

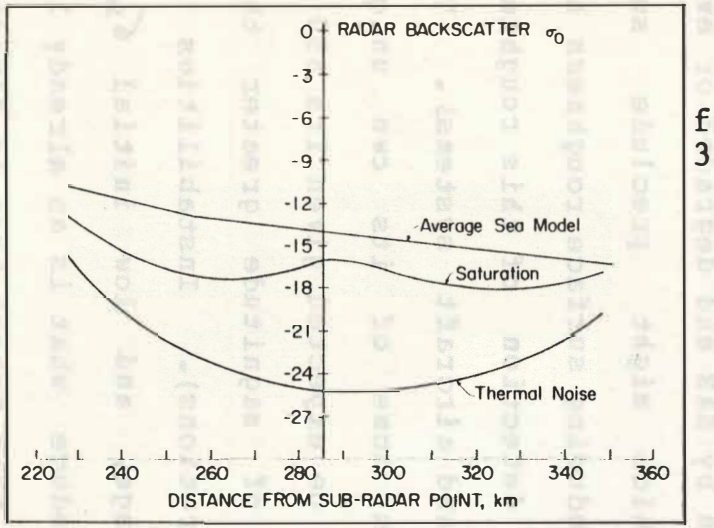

fig. 3.2

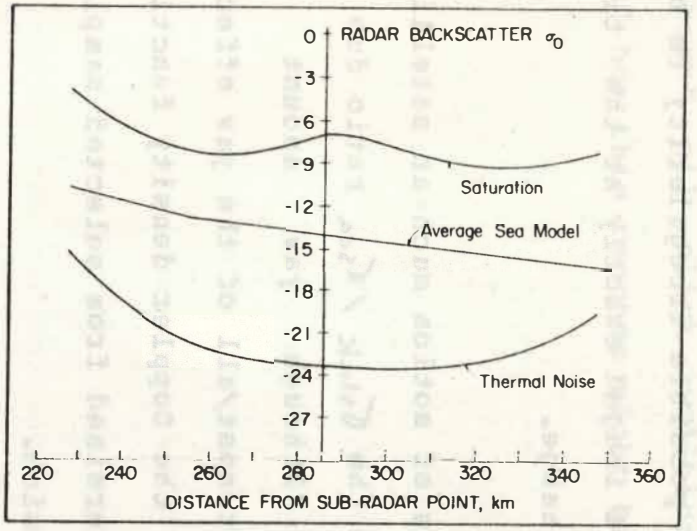

fig. 3.3

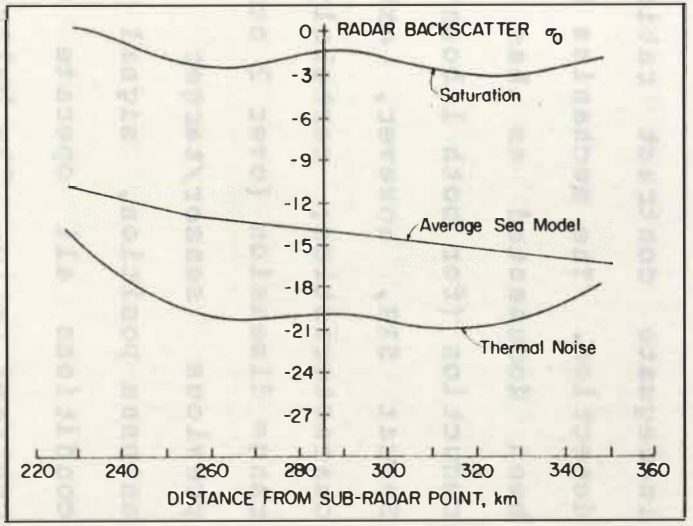

fig. 3.4

Figs. 3.2, 3.3, and 3.4 define the Seasat-A SAR system performance under three gain settings; high (95 dB), nominal (86 dB), and low (80 dB), respectively. The saturation curve represents values of σ which would drive the overall radar system to maximum detection levels. The thermal noise line represents the component of σ measured which is attributable to system noise. (Jordan, 1978)

satellite altitude during SAR imaging, linear features may be offset in azimuth. This possible irregularity is not pertinent for slick patterns not imaged exactly at the time of sudden spacecraft altitude change.

7.a Satellite yaw - Effects of motion such as satellitea yaw during imaging can decrease the $\sigma_{slick} / \sigma_{sea}$ ratio due to defocusing in processing. Although yaw amount is unspecified, it is assumed that most/all of the yaw effects can be measured on the basis of the Doppler density function and its center frequency as determined from selected samples of data before azimuth compression.

To summarize, the preceeding review establishes a case for both oil slick detection by SAR and degraded or even inadequate contrast ratios which might preclude such detection. The mechanism for reducing surface roughness has been documented as has SAR detection of this roughness reduction (for both laboratory and aircraft systems). The Seasat SAR, however, exhibits some of its own unique characteristics; certainly to be expected given its 850 km range dimension (over 2 orders of magnitude greater than previous sensor/target separations). Instabilities in antenna position, signal leakage, and low initial σ_{sea} conditions all operate to reduce what is an already low contrast ratio. The balance of this report then is directed

at establishing what the Seasat SAR's response has been to "known" oil slick conditions in the Santa Barbara Channel, and how this reponse might be uniquely characterized.

Trajectory Hindcasting

4.1 Introduction

As originally proposed, this research was to rely heavily on a large scale sea surface verification program. The failure of Seasat-A on October 10, 1978 before the initiation of regular experimental programs, however eliminated this standard proceedure, and cast some doubt on the fate of the entire research effort. It was subsequently learned that three imaging overpasses of the Santa Barbara Channel were completed by the Seasat SAR on July 18, August 4, and August 8. With these dates and satellite crossings times as reference the task of reconstructing oil slick conditions in the study area was begun.

4.2 Model Assumptions

The modeling of what initially would appear to be a totally random process in this instance has been greatly facilitated by the regular discharge of oil through the sea floor which occurs at specific points within the study area. The base map presented as fig. 4.1 outlines this primary seepage zone and its orientation with respect to the rest of the Channel. Observations of natural seepage within the

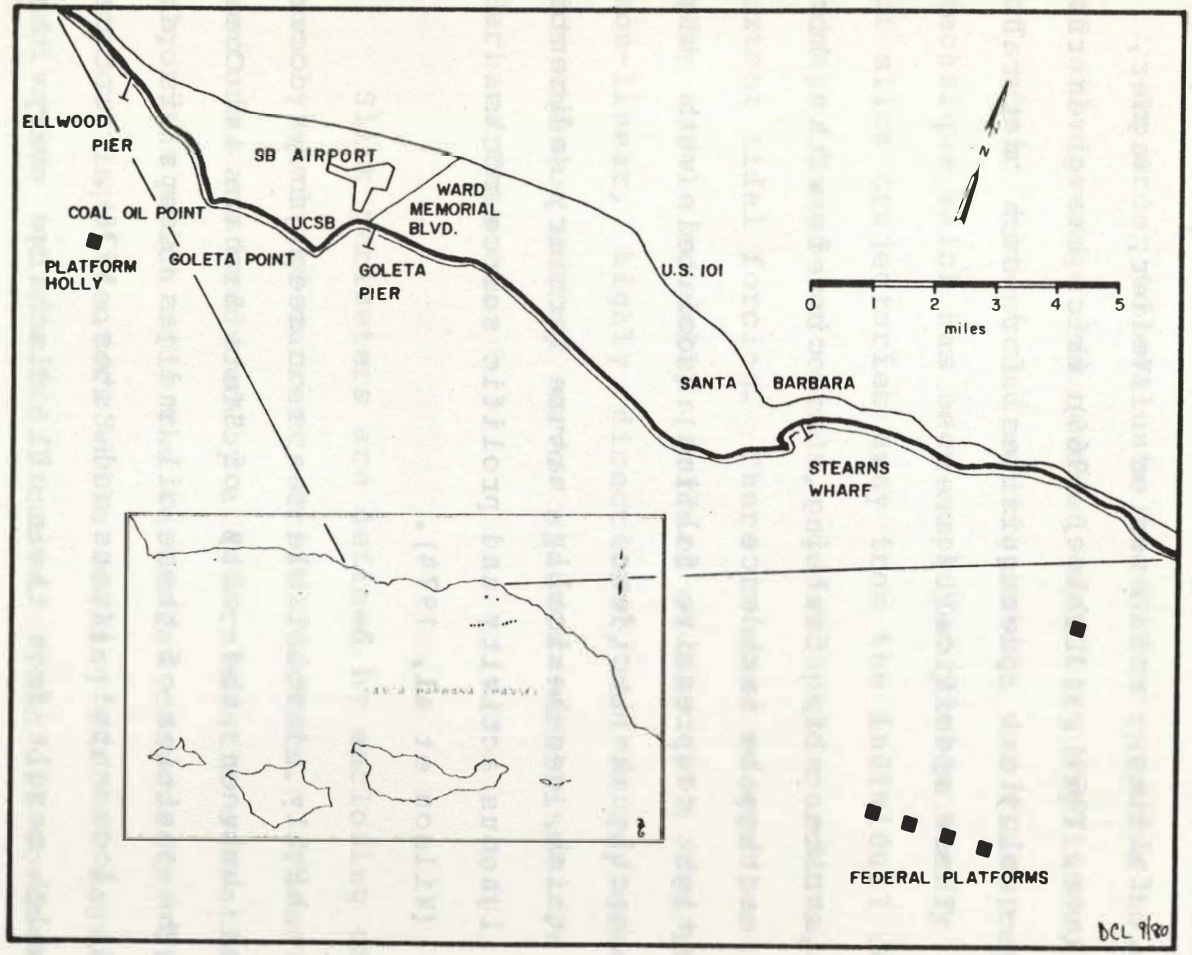

Fig. 4.1 provides a base map of the primary study area for orientation. Land features which are identifiable on the SAR imagery are labelled, as is the relative position of the study area with respect to the Santa Barbara Channel. The area covered by the map corresponds to that of subimages used in oil detection analysis.

area date back as far as 1868 (Imray, 1868).

Sandwiched between two major fault systems, the Santa Barbara Channel itself has undergone a complex sequence of faulting, folding, and erosion (Vedder, Wagner, and Schoellhamer, 1969), (Dibblee, 1966) which has given rise to all the geological prerequisites for such natural oil seepage. These specifically are:

1) strike slipe faulting associated with high earthquake incidence
2)e tight compressive folding associatede with high earthquake incidencee
3)e thick, geochemically mature Tertiary sediments;e and 4)e igneous activity and prolific source rockse (Wilson et al, 1974).e

Many highly identifiable seeps or seep groups occur in the area between the city of Santa Barbara and Coal Oil Point. The position of these oil and gas seeps is static and well documented (Kraus and Estes, 1976). Surface oil slicks which result from their oil discharge vary theough time from narrow streamers of a few hundred meters at one extreme to virtually continuous coverage of a ten to twenty square kilometer area on the other. The difference is largely a function of winds, currents, and tidal

fluctuation. A further source of variation is in the actual oil discharge rate from individual seeps, though this variation has not been quantified.

In order to evaluate the SAR's response to these areas of oil coverage and reduced capillary amplitude, an estimate of their extent and configuration was first required. The technique which has been employed yields hourly predictions of slick trajectories away from the individual seeps or seep groups based on winds, geostrophic currents, and to some extent tidal forcing. There is some suggestion that waves play a role as well, (Waldman et al, 1973) but the effect is non-linear, highly directional, and in any case negligable for the low energy wave spectra exhibited in the Santa Barbara Channel.

Slick perimeters are defined by enclosing end points of hourly wind and current drift vectors. These individual vectors are produced by a deterministic summation of forces algorithm which adds the Cartesian components of wind and current input vectors while scaling current magnitude by the derivative of the tidal curve. This oil movement algorithm is based on one developed for oil spill risk assessment by the United States Geological Survey (Samuels and Lanfears, 1978). Modifications have been incorporated which, for the purposes of this report will only be summarized. Details

are available in an unpublished Master's thesis by Wilson (1980).

Wind is input to the Samuels and Lanfear model on a statistically derived transition matrix basis. For the purpose of predicting oil configurations for a specific day and time, rather than overall averages, observed wind data has been interpolated from six points surrounding the study area. Three of these were located on the mainland (Santa Barbara Harbor, Oxnard Airport, and Santa Barbara Airport), two on the ocean (oil platform Hope and the drill ship Glomar Coral Sea), and one on Santa Cruz Island. The inverse square of the distance from the study area was used to scale the contribution from each site to resultant wind predictions. These predictions were generated hourly for the twenty four hour period preceeding each Seasat overflight.

The component of predicted surface drift attributable to wind has been calculated using linear assumptions arrived at empirically by several independent researchers (Schwartzberg, 1971) (Waldman et al., 1973) (Neu, 1970) and (Lange and Huhnerfuss, 1978). Wind drift magnitude is figured at 3.7 percent of observed wind speed while drift direction is shifted 20° to the right of observed wind direction to compensate for Coriolis acceleration.

Current information for the study area was obtained from the Bureau of Land Management's Outer Continental Shelf Study Group. The data consists of monthly average surface flow fields presented in polygon format (see fig. 4.2) Although nineteen separate sources were utilized in producing this data by far the dominant influence in determining flow regimes in the Santa Barbara Channel has been the drift card release and recovery work of Dr. Ronald Kolpack of the University of Southern California.

In its original format this current data was difficult to utilize for oil trajectory simulation on the relatively small scale required. A single polygon covers nearly the entire study area (boldfaced polygon in fig. 4.2) and sharp discontinuities exist in the flow field from one polygon to another. In addition, significant components of the flow in several areas lie orthogonal to the land boundary. To correct these problems an interpolation algorithm was developed which solved LaPlace's equation ($\nabla^2 V = 0$) in two dimensions yielding smooth discretized current fields with well behaved flow along the land boundaries (see fig. 4.3). In addition, a continuity constraint was included in this algorithm such that flow across the free (non land) boundaries was normalized.

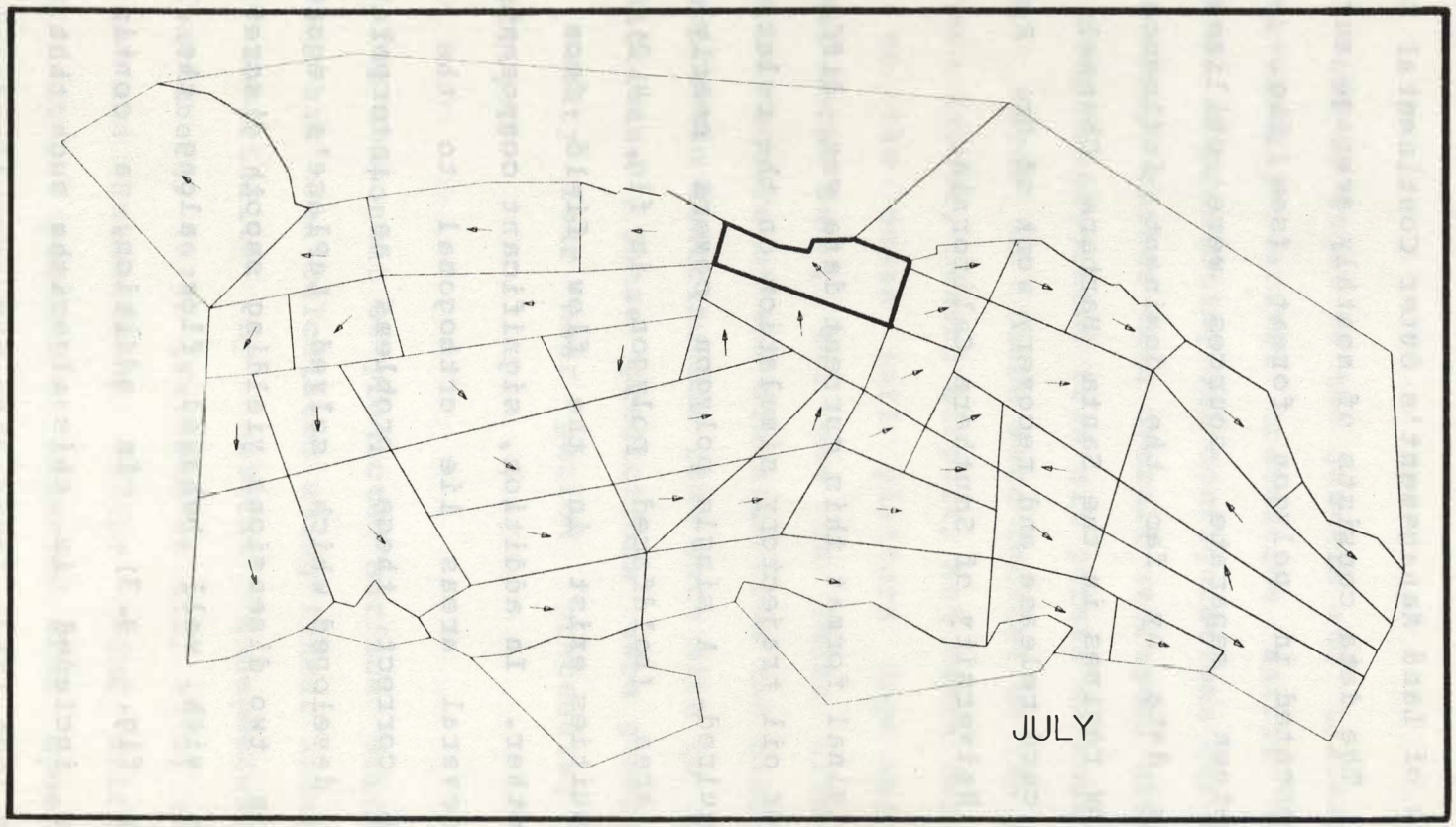

Fig. 4.2 depicts surface current flow fields for the month of July in the Santa Barbara Channel. Source of this data is the Bureau of Land Management, Los Angeles, Outer Continental Shelf Study Group. Boldfaced polygon represents roughly the same area as the base map (fig. 4.1).

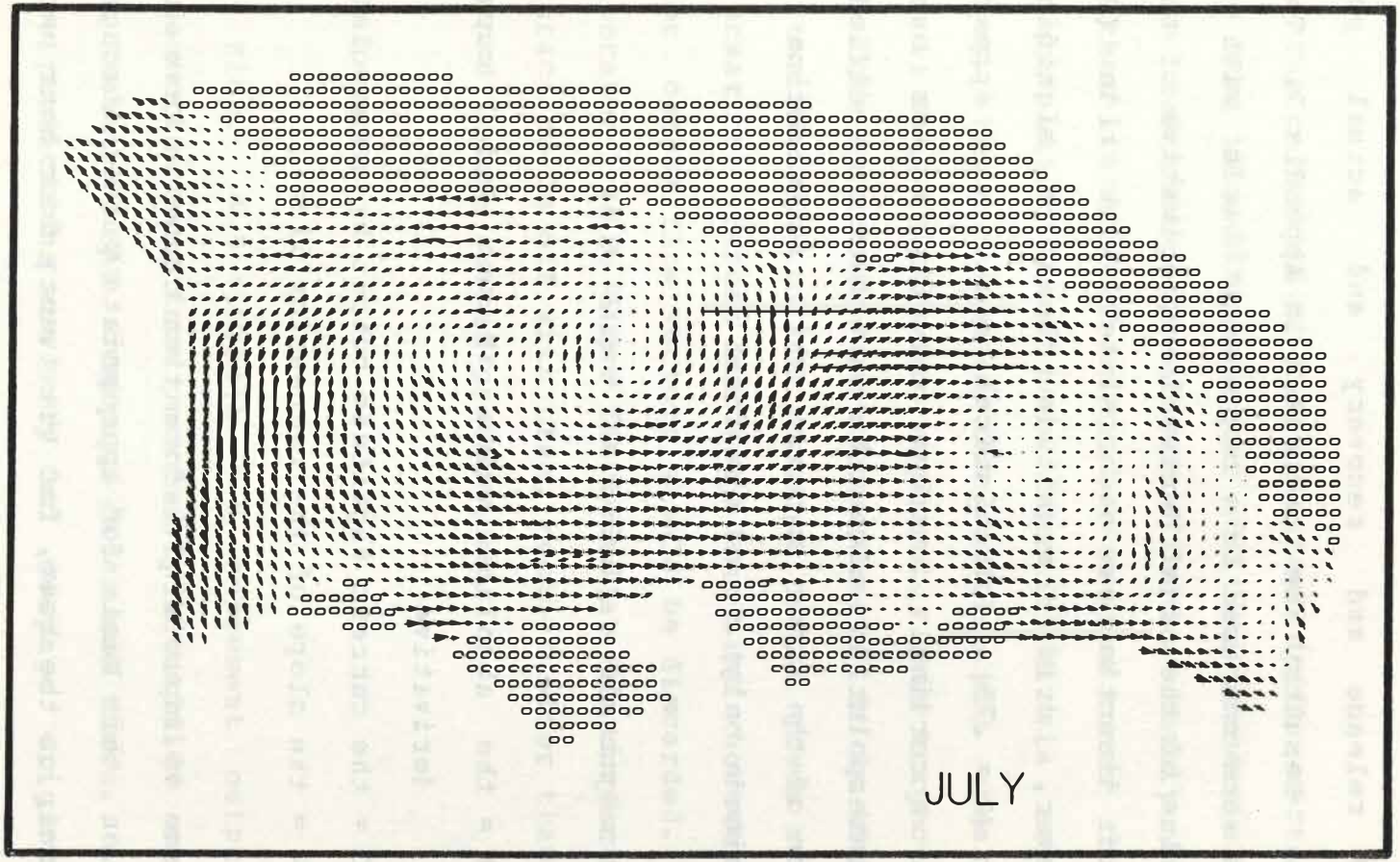

Fig. 4.3 shows the July surface current field for the Santa Barbara Channel after interpolation using a LaPlacean operator. Continuity is maintained in the flow field, and zero flow through land boundaries is specified.

Finally, in considering tidal effects a series of nineteen observations of current velocity were taken via drift board release and recovery and actual point measurement. Results are presented in Appendix 1. These observations were compared on a regression basis with the absolute value of the tidal derivative (derivative of tidal curve). Drift direction was uncorrelated with tide (R = .20), however, drift magnitude showed a significant relationship (R = .75). (Statistical results also appear in Appendix 1). Accordingly, current velocity values output from the interpolation algorithm are further modified by consideration of the tidal cycle. This modification (to current magnitude only) is of the form:

current magnitude = (1.58 * C) + (.24e* A)e

where A = the absolute value of the tidal curve derivative

C = the current magnitude output by interpolation

and .24e = the slope of the regression line.

As in the case of input wind information currents have been calculated on this basis for appropriate points throughout the study area, on the hour, for the twenty four hour period preceeding the Seasat overpass times.

4.3 Component Summation

The calculation of a resultant drift vector for each time step is a simple vector addition process which overlays these calculated component effects. Hourly output vectors are then linked head to tail away from zones of consistent seepage which have been identified via repeated aerial survey. Fig. 4.4 shows the position and areal extent of the oil seep features so employed. This trajectory modeling technique is termed "weathercocking". It is highly accurate in the vicinity of the point of origin given reliable input information. Errors multiply over time however such that older output flow vectors should be discarded. As much oil evaporates in the first few hours at the surface and since accuracy tails off with time, vectors older than 8 hours are dropped in the output predictions.

4.4 Results

Figs. 4.5 through 4.6 represent output predicted trajectories away from previously identified seepage zones for Seasat-A SAR overpass dates and times. As mentioned, these predictions are only for seepage originating within the most recent eight hours. This provides an initial cause to suspect underestimation. The trade off is a reasonable

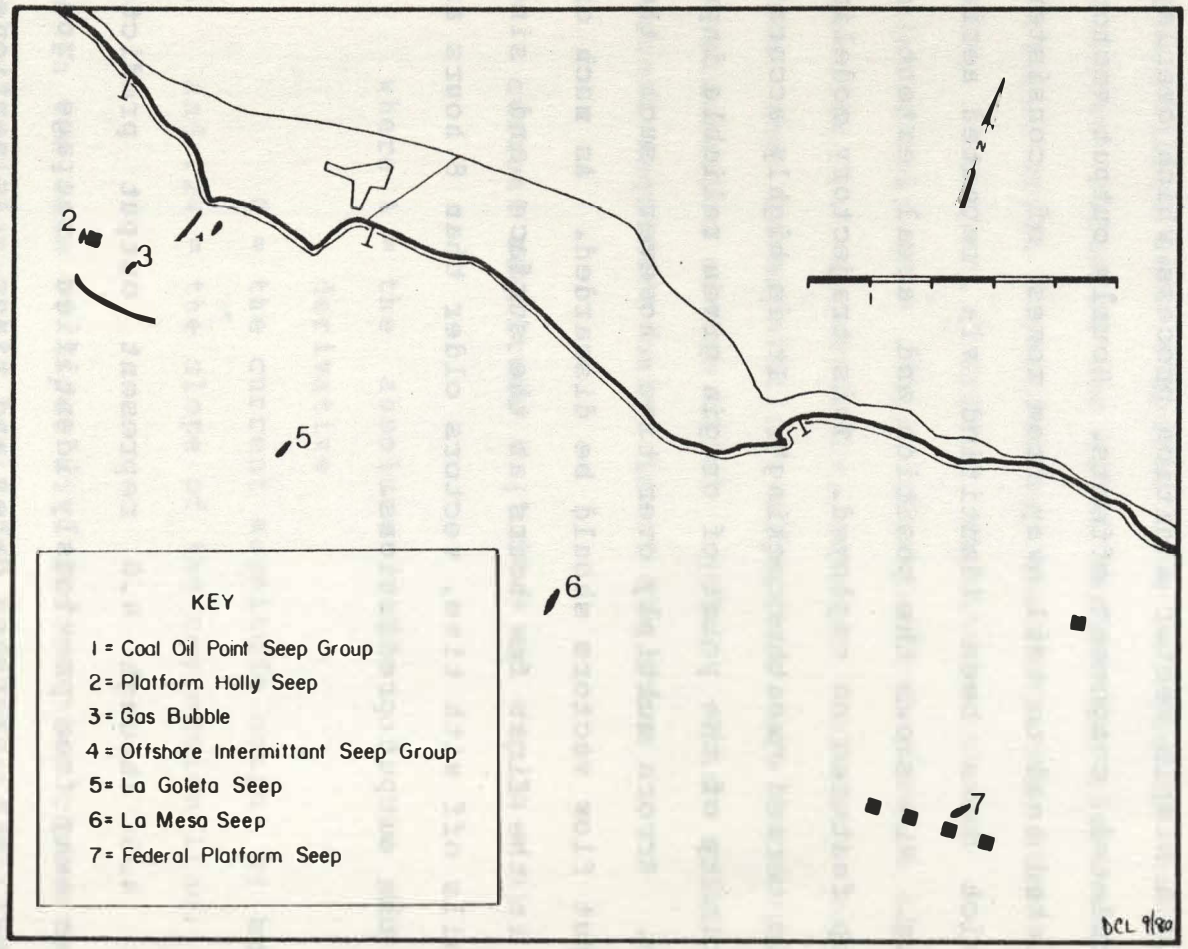

Fig. 4.4 identifies and locates the seven promary oil seeps and seep groups which have been utilized as points of origin for plotting predicted oil slick trajectories

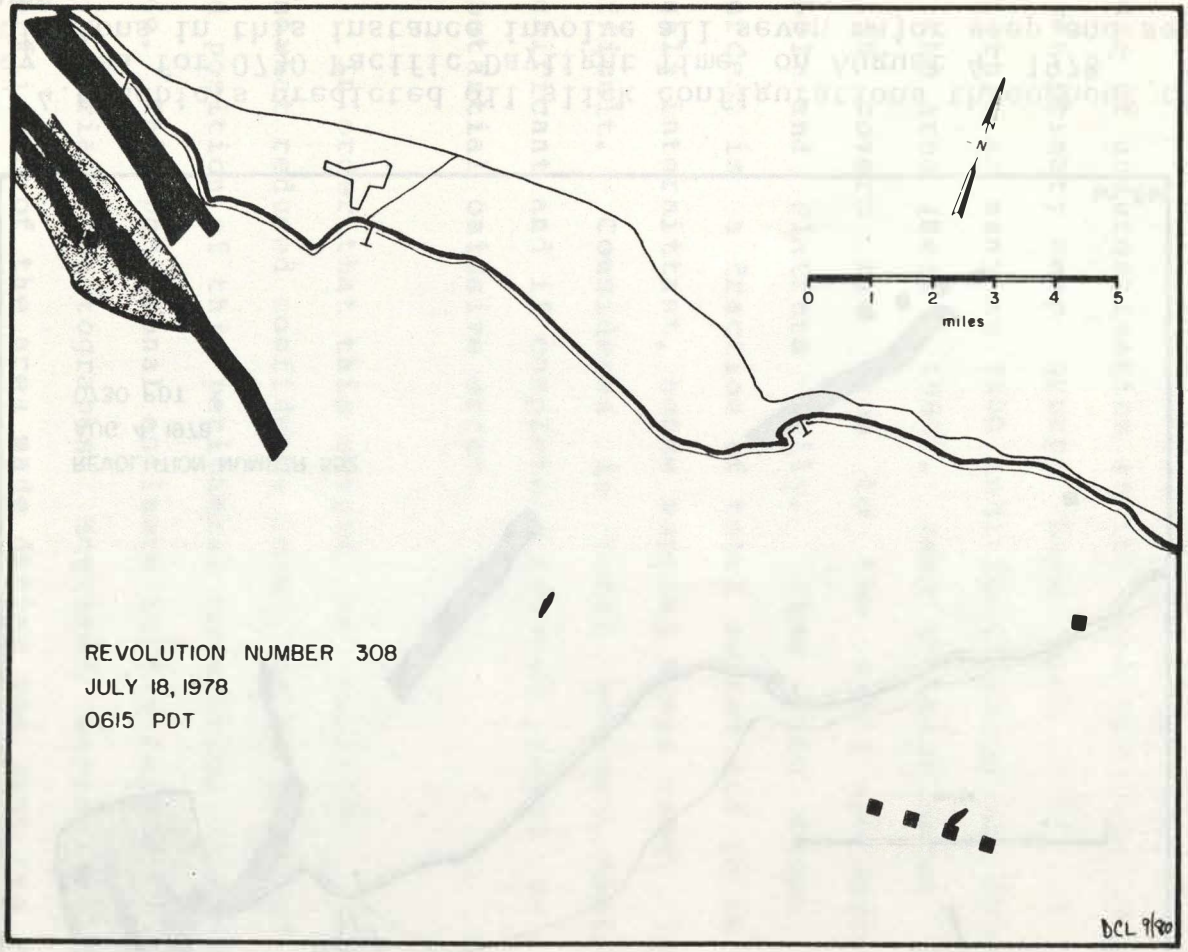

Fig 4.5 depicts predicted oil slick configurations in the Coal Oil Point vicinity for 0615 Pacific Daylight Time, on July 18, 1978. Predictions for the La Mesa and Federal Platform seeps have been deleted. Lighter toned slicks represent output from the Intermittant Offshore seep group.

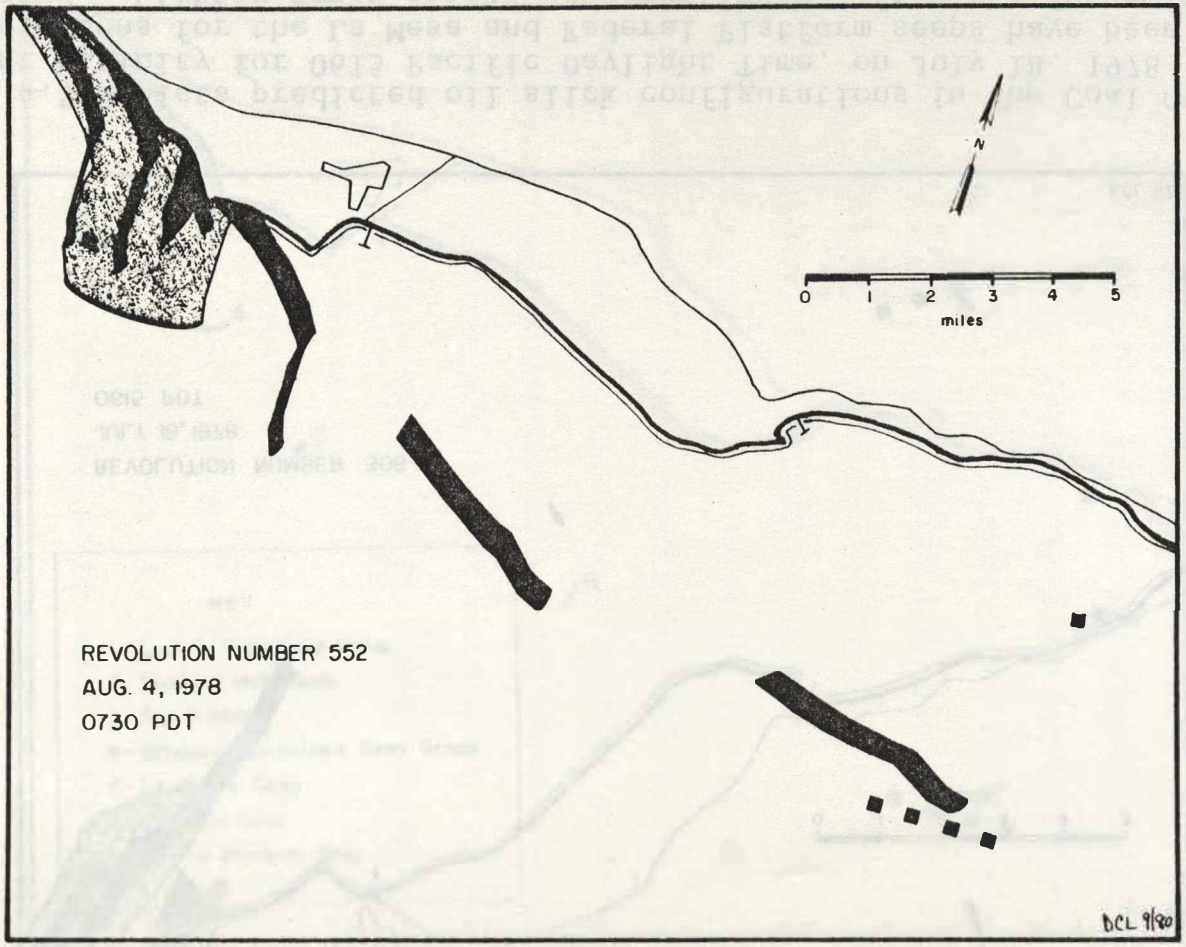

Fig. 4.6 depicts predicted oil slick configurations throughout the study area for 0730 Pacific Daylight Time, on August 4, 1978. Predictions in this instance involve all seven major seep and seep groups.

confidence that errors of comission have been minimized, a fact which will prove vital in image processing.

An attempt has been made in the display of these oil coverage predictions to reduce the effects of a further cause of underestimation at the Coal Oil Point site. Though seven primary seep groups have been used as points of origin, as many as 1400 individual seeps are known to exist in the area (Reitz, 1980). Many of these occur in an arc which covers the area to the south and east of the gas bubble and Platform Holly. Flow from these individual sources is a fraction of total output and is in most cases highly intermittant, hence mapping their exact location is difficult. Considered in total however, their output is significant and if completely ignored would be cause for substantial omissive error.

In order that this output be included, albeit at a somewhat reduced confidence level, an estimate of the extent and position of this peripheral collection of seeps has been made. This positional estimate is the result of examination of aerial photographs acquired during nearly thirty overflights of the area made during the past two years. Two examples are included as figs 4.7 and 4.8. Oil configurations associated with this group have been calculated via the same previously described modeling

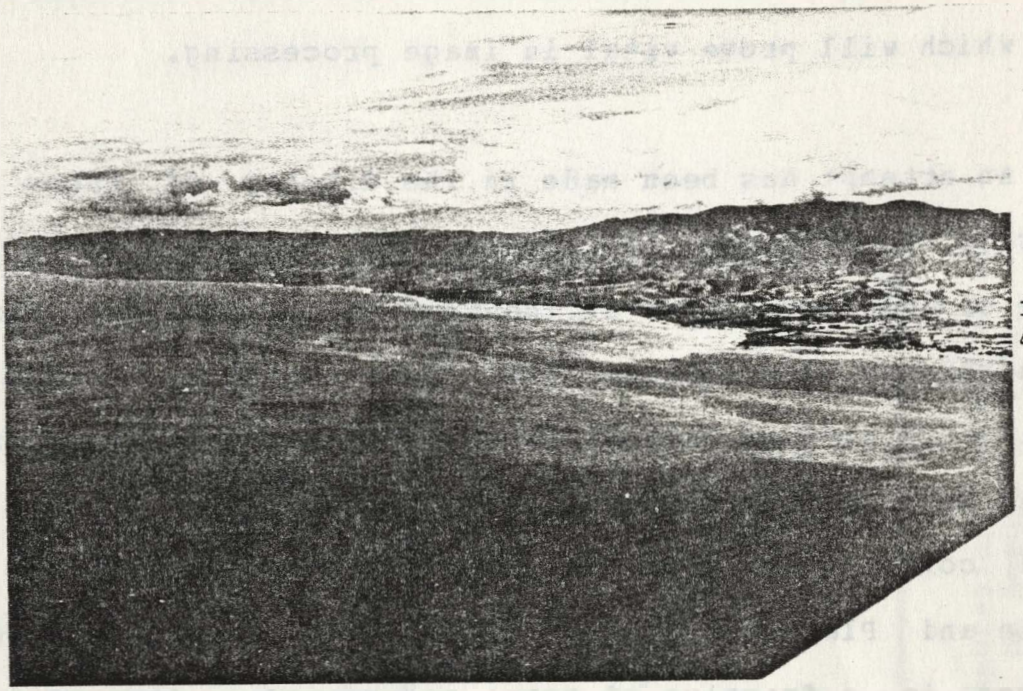

fig. 4.7

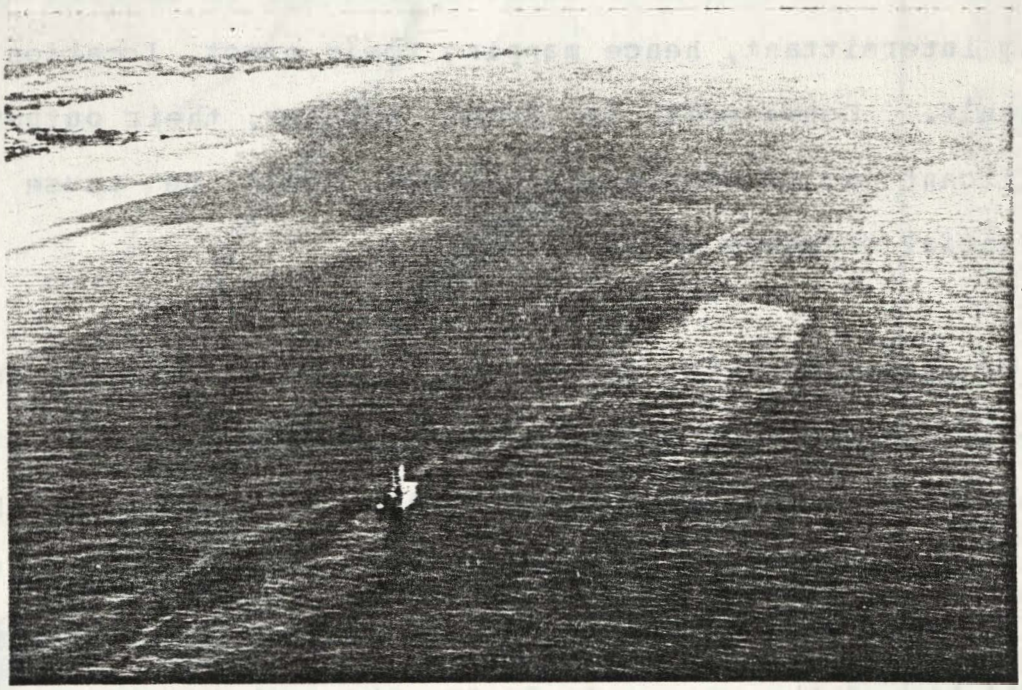

fig. 4.8

Figs. 4.7 and 4.8 are both aerial panchromatic photographs of the Coal Oil Point area, taken towards the east and northwest, respectively. Oil discharge from the spatially variable Intermittant Offshore Seep Group can be seen in the right margin of fig 4.7 and as the nearest lighter toned (oil slick) feature in the foreground of fig.4.8.

techniques. For graphic display, however, these slicks have been differentiated by a lighter tone (see figs. 4.5 and 4.6).

4.5 Accuracy Analysis

As a test of the mechanical assumptions incorporated in the trajectory model, five comparisons were made during the summer of 1980 between predicted and observed drift. Test results appear in Appendix 2. Due to sampling time limitations, comparisons are based on measurement of instantaneous drift only. Using the modified BLM current data (modified by tidal derivative) and wind observed on-site, a predicted drift vector was calculated for the Platform Holly area. Drift was simultaneously measured at the site via a Teledyne Gurley cable suspended current meter.

In two cases directional predictions were within two degrees of those observed. In two more the error was within 20 degrees, and in one case it was 48 degrees. During this latter instance winds were uncharacteristically strong (12 knots) and dominated flow. Drift magnitude estimates were generally within a $\pm$ 0.1 to 0.3 knot range of observed flow which is near the advertized accuracy of the meter.

Given an average observed drift of .38 knots in the study area, and an average directional error of 20 (obtained from these tests), a mispositioning of trajectory endpoints of up to one nautical mile would be expected at the end of 8 hours. Two factors which might serve to mitigate such error are that: 1) No spreading coefficient is incorporated in predicted trajectories, and 2) Narrowly defined points of origin are employed. Though these factors may be further cause of omissive error, no reliable quantitative means of evaluating their effect has been devised. In any case, given the inevitable base level of noise in model predictions and a requirement of minimizing misidentification of oil (comission), the conservative approach outlined herein is deemed most appropriate.

Image Interpretation

5.1 Data Quality

Of the three Seasat-A SAR overpasses which cover the Santa Barbara Channel only two have proven useful within the context of this research. Revs 308 and 552 are both ascending mode images (platform moving south to north) of good quality which cover the entire study area. Rev 617 is a descending mode (north to south) overpass which exhibits extremely low dynamic range (and therefore reduced potential for ocean surface feature detection). The reduced contrast ratio is the result of a very low gain setting. Additionally, the satellite track for this image is positioned such that the SAR swath covers only the eastern portion of the study area. Efforts to expand (stretch) the image's apparent grey level range and thereby improve feature differentiation in oceanic sub images have produced concommitant increases in harmonic noise. As final image processing proceedures involve spatial frequency transformations, this high coherent noise level in the digital data was deemed unacceptible. Rev 617 has accordingly been dropped from consideration.

Figs 5.1 and 5.2 are subimages of the study area extracted from revolutions 308 and 552 respectively. These

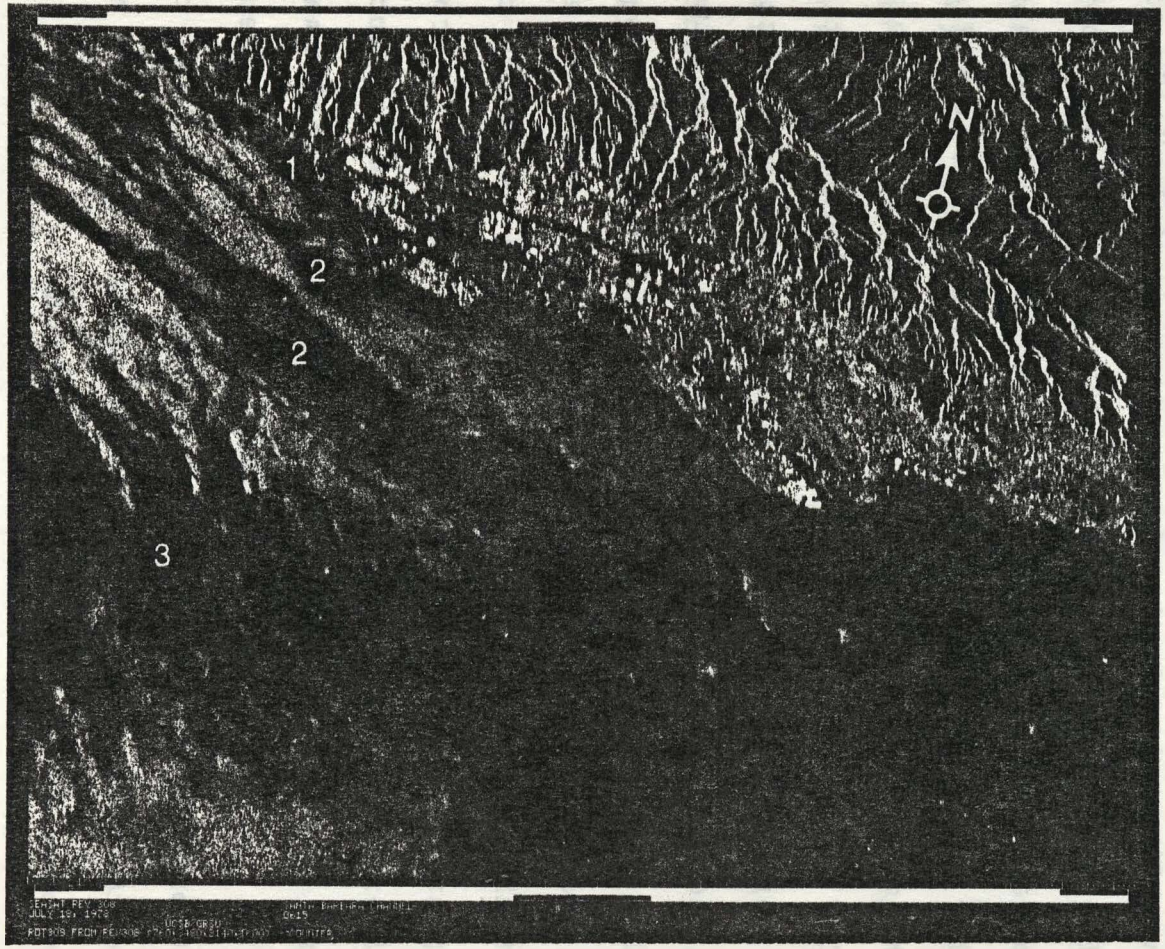

Fig. 5.1 is a rotated subimage of the study area taken from Seasat Rev 308. Numbers on the image identify different reduced backscatter targets which are separately described in the text.

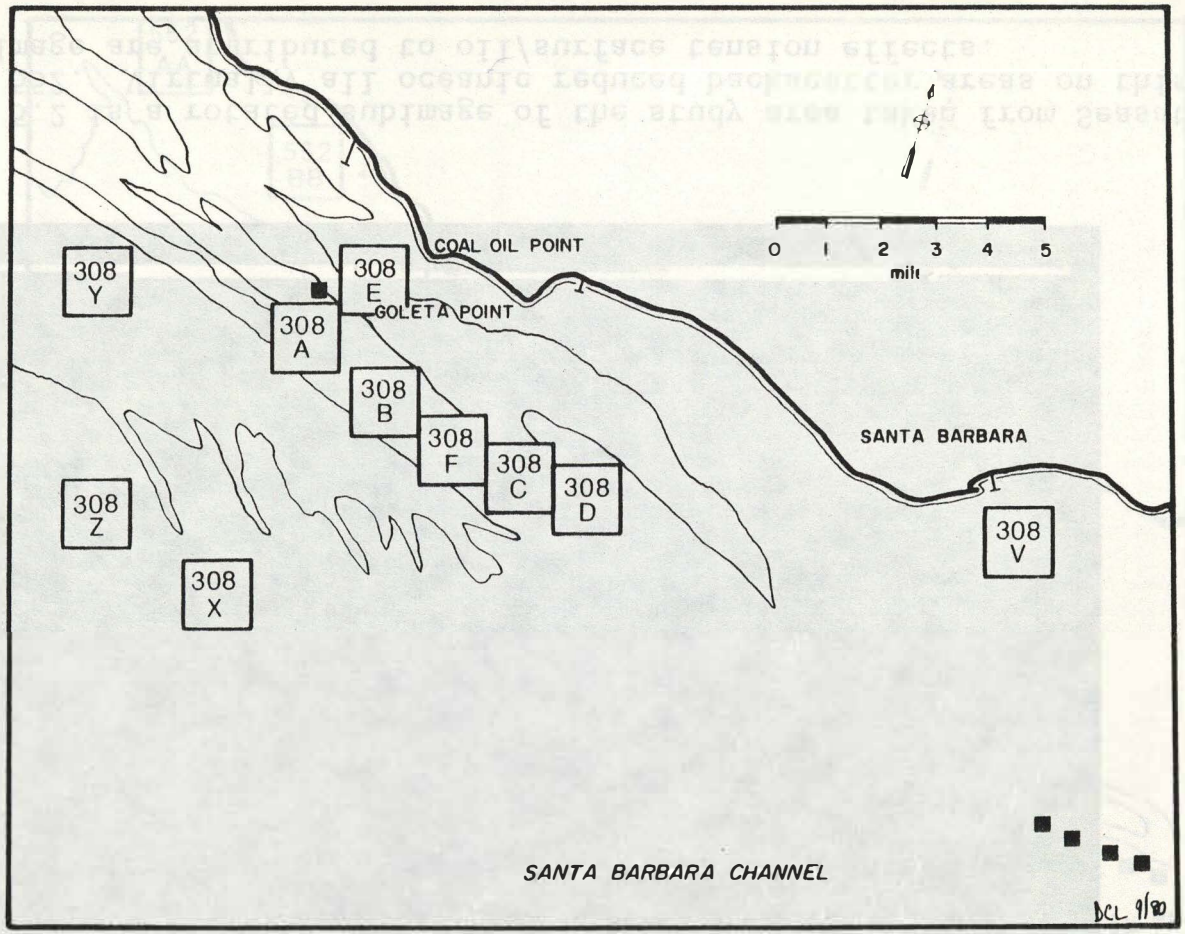

Fig. 5.1A shows the relative position of 128 X 128 pixel, oil affected and non-oil affected subimages taken from Seasat Rev 308 SAR imagery. This figure superimposes positionally on fig. 5.1. Subimages are used in subsequent spectral analysis image processing.

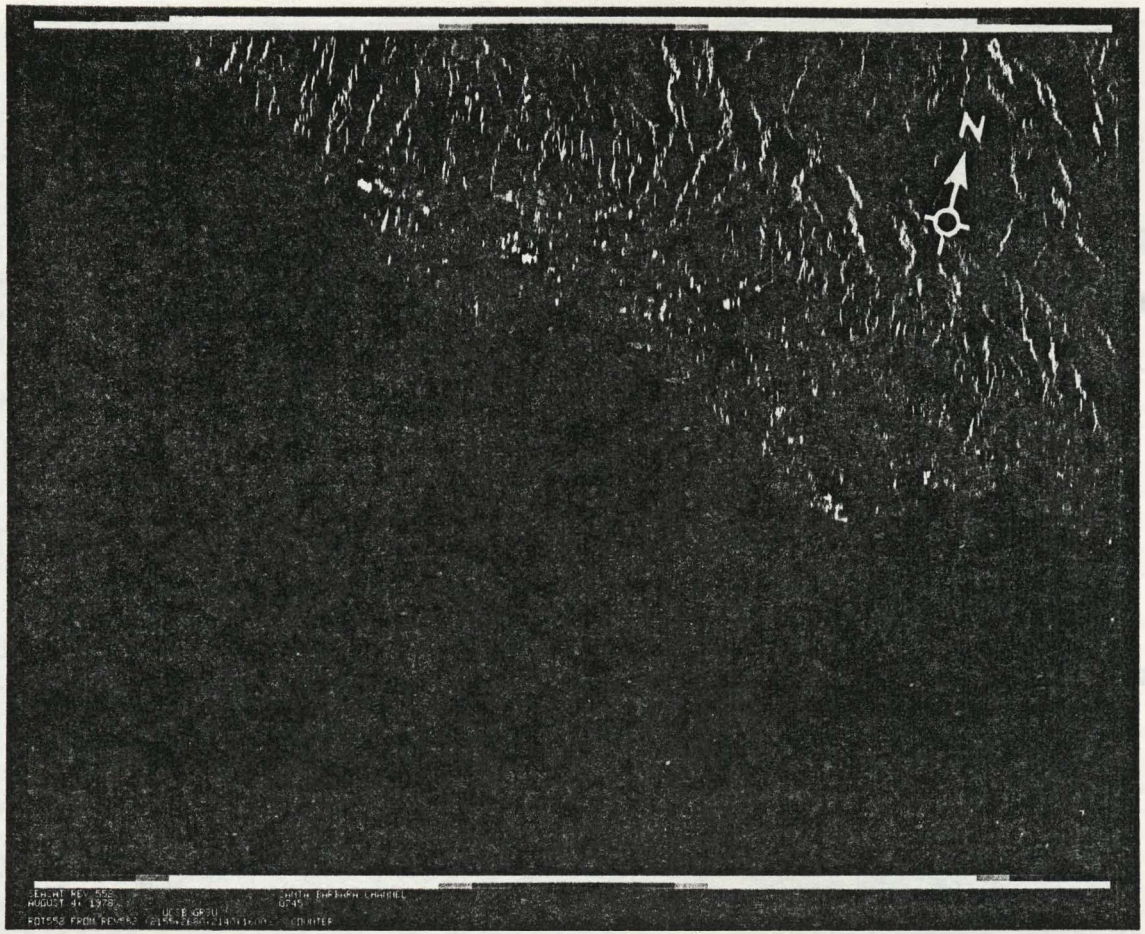

Fig 5.2 is a rotated subimage of the study area taken from Seasat Rev 552. Virtually all oceanic reduced backscatter areas on this subimage are attributed to oil/surface tension effects.

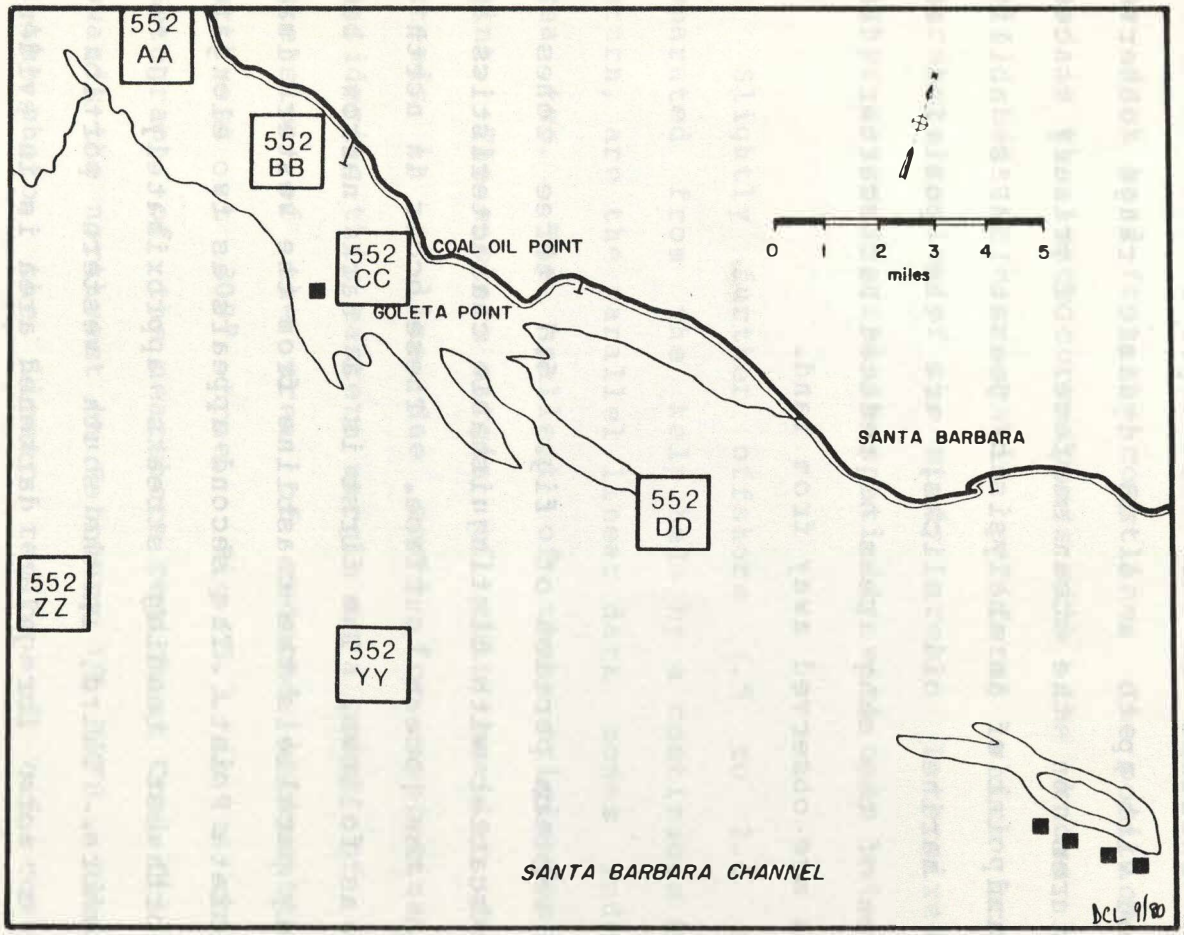

Fig 5.2A shows the relative position of 128 X 128 pixel, oil affected and non-oil affected subimages taken from Seasat Rev 552 SAR imagery. This figure superimposes positionally on fig. 5.2.

digitally correlated scenes correspond in area to that depicted in the map included as figure 4.1. For orientation, land features which are identifiable in the imagery are included in this base map. In both subscenes focus is good with up to a 6 dB dynamic range observed across features on the ocean surface. Of primary concern from the standpoint of an analysis of Seasat SAR's ability to detect marine oil slicks, are the position and configuration of the many areas of reduced backscatter (dark areas) which are observed away from land.

5.2 Rev 308

In the western portion of fig. 5.1 three zones of reduced backscatter with distinguishable characteristics are apparent on the ocean surface. These occur in north to south order as follows. The first is a dark narrow band which closely parallels the coastline from the western image margin to Goleta Point. The second appears as two elongated parallel northwest tending streaks approximately 1 to 4 miles from shore. Third, in the south western portion of the image a more irregular darkened area is in evidence which exhibits a "saw tooth" northern boundary. These features are identified by number on figure 5.1.

Within the first feature, from its western extremity to Goleta Point several small pockets of higher backscatter (brighter return) are interspersed , while to the east of Goleta Point a single larger zone of higher return divides the dark band from the coastline. The position of the dark band in the image corresponds with the known location of kelp beds (Macrocystis pyrifera) which occur in the nearshore region of the study area. Intermixed zones of higher return correlate spatially with open water.

Slightly further offshore (.5 to 2.00 miles) and separated from the kelp beds by a continuous band of high return, are the parallel linear dark zones indentified as area two. The smallest of these originates at Coal Oil Point. The eastern margin of this smaller dark feature extends in a line due south for approximately 1 mile. Considering this eastern margin as a point of origin, the extension of the area of reduced backscatter is to the northwest at 300^{8} true. Fig 5.3 is a color aerial photograph of the nearshore region at Coal Oil Point taken towards the northwest on February 18, 1978. Clearly visible on the photo, the linear regiono of oil coverage which corresponds to an area of known natural seepage extends from the left (southern) margin of fig 5.3 to the tip of Coal Oil Point. The area covered by what is interpreted to be oil in the photo (fig 5.3) corresponds positionally with the

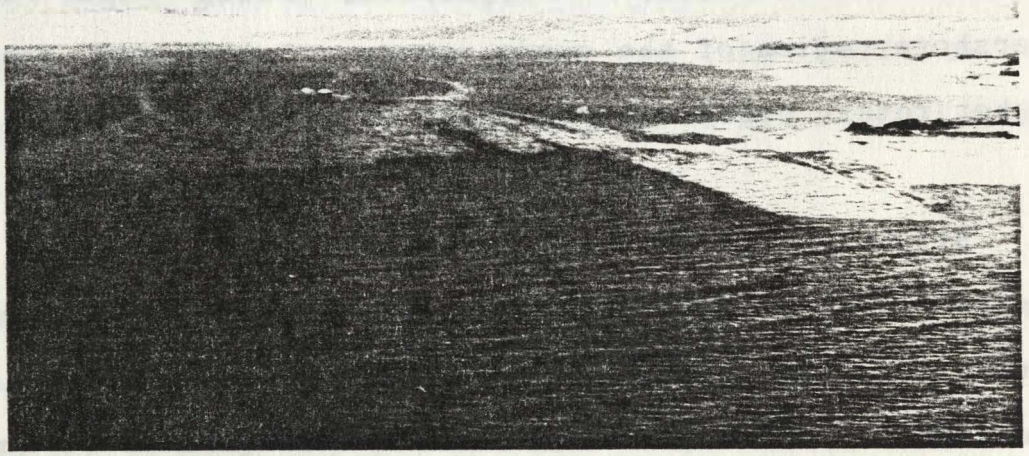

Fig. 5.3 is a color aerial photo of the Coal Oil Point area which shows clearly the linear point of origin associated with the Coal Oil Point seep group (number 1 in fig. 4.4). Camera heading for this photo is northwest.

smaller inshore dark component of area two on the radar data. Note as well the similarity in the manner in which both radar and visible image oil slick features narrow to a ribbon like pattern in their western extremity.

Within area two an identically oriented but larger zone exhibiting reduced backscatter is positioned slightly further off shore. Near the northern margin of this feature, and to the southwest of Coal Oil Point, a single bright dot represents the return from the Atlantic Richfield oil platform Holly; a metal structure approximately 50 meters on a side and extending 35 meters above the sea surface. As stated, this larger zone of low return exhibits the same 300° true orientation however, its overall position does not correspond as precisely with a single differentiable oil seep. Rather, it brackets an area which contains several of the major seep groups as well as much of the peripheral area which exhibits intermittant seepage. This larger portion of area two, in its eastern extension expands, joining with the third low return feature from the south to form a continuous dark band from the shoreline out nearly 12 miles, effectively masking any oil slick signature which might be produced by the small Federal Platform seep.

For image processing purposes which will be discussed in section 6, subimages of features attributed to both oil

slick effects as well as similar appearing but non-oil related "confusion targets" are required. Oil coverage subimages 308A, 308B, 308C, 308D, 308E, and, 308F are examples of the former taken from area two. Their relative positions are noted in fig 5.1A. Again it should be emphasized that confidence in the selection of these subimages is enhanced by a combination of: 1) documentationa on the known position of natural seeps within the Santa Barbara Channel, (Kraus and Estes, 1976) (Kraus et al., 1977) (Wilson et al., 1979) and 2) the verified utility of mechanical assumptions employed in the oil trajectory prediction model.

The third zone of low backscatter is separable only in the south western portion of the subimage, where its previously mentioned saw toothed northern margin differentiates it from area two. The nebulous nature of this boundary, along with the feature's position well away from known areas of natural oil seepage indicate that the low return here is more likely attributable to vagaries in the wind field than oil/surface tension effects. Accordingly, this area has been used in image processing oil slick detection studies to provide subimage examples (308V, 308X, and 308Z) of non-oil attributable confusion targets.

The trajectory model prediction of oil slick

configuration for this day and time is given in the previous hindcasting section (fig 4.5). Agreement is quite good with an average slick heading towards 308° true predicted for the most prolific and reliable seep groups, near Coal Oil Point. Predictions have not been formulated for the more easterly seeps as backscatter in their vicinity is uniformly low on the Rev 308 imagery.

For reference, wind was light and variable at around 4 knots from 120° true during this overpass (July 18, 1978 - 0615 PDT). Fog covered much of the Channel. Tide was incoming and seas were nearly calm with a one foot swell from the west/southwest. Current set in the Coal Oil Point area is estimated at .7 knot towards the west/northwest (313° true).

5.3 Rev 552

Obtained August 4, 1978, Rev 552 represents the most finely focused Seasat-A SAR data available for the Santa Barbara Channel. A uniform medium backscatter covers most of thes channel study area, with the exception of a single large zone of low return which starts 5 miles west of Coal Oil Point extending 8 miles further up the coast and nearly 15 miles offshore (see fig. 5.4). Though its origin is unknown, the feature is certainly not attributable to oil

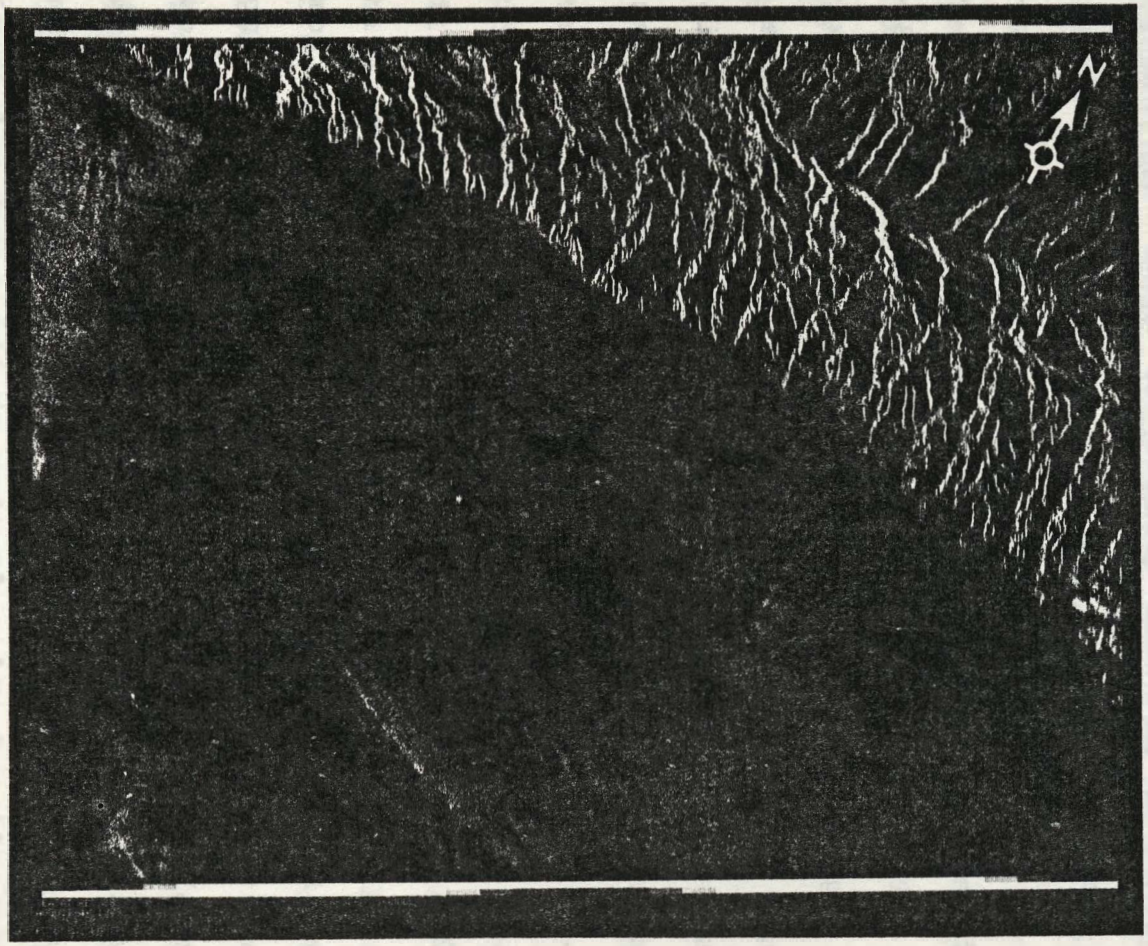

Fig. 5.4 is a rotated subimage from Seasat Rev 552 SAR imagery. The postion of this scene is due west of the subimage presented as fig. 5.2. An overlap of approximately 35 % can be observed by comparying the two images.

coverage. It is too large to have gone unreported. Further, it is well out of the zone of prolific seepage and does not exhibit the abrupt boundaries and sinuous pattern of oil/surface tension related signatures. Rather it shows gradation in tone from high to low return. We have accordingly employed this region in obtaining confusion target subimages (552VV, 552XX) for comparison with backscatter reduction signatures which have been attributed to oil coverage (see fig 5.2A). Several of the latter such signatures occur on this image in both the vicinity of Coal Oil Point as well as further to the east (552AA, 552BB, 552CC, and 552DD).

As can be seen in fig. 5.2 the Coal Oil Point nearshore region is largely blanketed byoa single continuous band of low return. Oil trajectory predictions for this date and time show a northwesterly drift away from primary seepage zones which would account for the uniform signal reduction (see fig. 4.6). In this instance the suggestion is that oil plumes have merged with the signature of nearshore kelp beds, reducing surface roughness all the way to shore. An exception appears to occur at the western terminus of the backscatter reduction zone which originates at Coal Oil Point, where what is interpreted as an oil slick plume has pulled a small distance away from the positionally stable kelp bed signature.

Further offshore, in the area previously defined as a zone containing a large number of individual seeps of variable productivity, several smaller streamers of reduced surface roughness (low return) are observed. These plumes on the the imagery show a heading of 310° true which compares with a model prediction of 320° true for this portion of the study area.

Two additional, and more prominant streamers of low backscatter are present still further to the east with eastern points of origin corresponding to the location of the La Mesa seep group and the Federal Platform seep (see figs 4.4 and 5.2). These features, interpreted as the result of natural seepage, exhibit mean headings of 290° true and 275° true respectively on the imagery. Model predicitons for these areas are displayed in Fig 4.6 showing corresponding mean headings of 302° true and 288° true. Subimage 552DD is taken from the La Mesa seep area, however, the slick issuing from the Federal Platform area is not of sufficient dimension to permit creation of a representative subimage.

Closer examination of the Federal Platform seep on the SAR imagery reveals that in the immediate vicinity of its origin a heading of roughly 20° true is observed. The model

prediction does not reflect such a rapid shift in drift direction. This particular predictive error at high frequency (spatial) is likely attributable to lack of accurate wind data near the site (Platform Hope anemometer was not operational during this overpass). In a broader sense however this error is characteristic of the expected inadequacies of coarse scale driving data when utilized in a spatially interpolated format to predict finer scale events. The suggestion is that the mean heading approach which has been employed in these interpretations is likely the limit to which the so called "surface truth" data generated herein should be employed.

At the time of overpass (0730 PDT) wind was 5 to 7 knots from 240° true. Tide was strongly incoming and seas were calm. A 1 to 2 foot swell was moving from the west/southwest. Estimated current set was 287° true at the Federal Platform seep, 303° true at the La Mesa seep, and 331° true at Coil Oil Point. Drift speed at all three sites was approximately .5 knot.

5.4 Image Interpretation Conclusions

These interpretations have, by design centered only on oceanic features. Additionally, analysis has dealt with only those features within the confines of the described

study area. The purpose is not to oversimplify, but rather to focus on the central research question of Seasat-A SAR's sensitivity to oil slick related surface effects in the marine environment. A lack of concurrent field verification data has hampered analysis and has necessitated the use of current, wind, and tidal information, as input to a model which sums these driving forces, to predict the movement of surface oil slicks away from well documented points of origin. Examples of aerial photography have been included which are selected from numerous flights, all of which reinforce the interpretation that many of the observed areas of reduced backscatter on the radar imagery are attributable to the presence of oil. Although circumstantial, the weight of this sort of corroborating evidence is substantial.

A significant problem remains, however, in that aside from some manual and subjective qualitative pattern recognition criteria no reliable means exists of separating bona fide oil slick signatures from similarly darkened areas which are not the result of oil/surface tension effects. It has been our intent to explore more quantitative means of separating these so called confusion targets using digital image processing techniques which capitalize on the frequency specific roughness-reducing action of oil. Efforts in this area are discussed in the following section.

Image Processing

6.1 Introduction

Oil slick identification employing Seasat-A SAR imagery focuses on the potential for discrimination of oil slick caused, low backscatter regions from similar appearing ocean surface features (so called confusion targets). The concern is thus to develop a methodology which detects any significant differences in those portions of a SAR image which represent low or reduced backscatter regions caused by oil slicks, as compared to other image features which createa similar amplitudes and spatial patterns.

The application of spectral analysis for the comparison of Seasat SAR imagery of normal and oil slick affected waters was considered a logical, but not entirely promising postulate. This is because "although oil is known to suppress the capillary waves, quantitative information on the amount of suppression of the radar backscatter at most frequencies is not available" (Moore and Fung, 1979). Further, though it is generally accepted that SAR images of ocean swell are due primarily to the presence of capillary waves whose brightness on the final image is determined by swell slope, capillary dynamics, Doppler and focus modulations, there is no consensus on the balance of

mechanisms governing these effects (Raney and Lowry, 1978).

In addition, some scepticism concerning the ultimate potential of spectral analysis for oil slick discrimination stems from the fact that Seasat imagery has a spatial resolution significiantly below the ocean wave capillary frequencies dominantly affected by slicks. Since the effect is expected to range between subtle and non existent or to be lost in spectral noise, a direct comparison of the Fourier transform of slick vs. non-slick Seasat subimages would probably be insufficient. Power spectrum averaging is thus required to enhance subtle differences in the transforms of ocean regions imaged near the system noise level. For discrimination in areas whose signal is near this noise level, concern would be to guard against spurious spectral differences forced by insufficient sampling and averaging. Otnes and Enochson (1978) note that difficulties may arise if spectral power density estimates are performed without proper care, and that statistically inconsistent estimates result when no frequency smoothing is performed.

6.2 Spectrum Power Analysis

The utility of spectrum power analysis for frequency selective, detection signatures of relatively low energy physical phenomena has been prominent at least since the

major work of Blackman and Tukey (1958). Later, computer implementation of the Fast Fourier Transform (FFT) expanded the application of such analysis. Recently, one significant variant of maximum entropy spectral analysis, the semicausal model, demonstrated improved frequency discrimination (by a factor of about 2 1/2 along with attenuation of the dc spectral component) for small data sets (Schuchman et al., 1979). The resolution limit (Δf) of a standard Fourier transform (in spatial frequency or cycles/sample) is about $\Delta f = 1/\Delta t$ where Δt is the length of the data segment (Shuchman et al., 1979). When Δt = 128 samples at 25m/sample, Δf = 1/128 = .0078 cycle/sample = 3.125E-4 cycle/m.

Fourier transforms of images may be one or two dimensional. The result of a one dimensional transform is power as a function of spatial frequency. The directional orientation is in either the line or sample direction in accordance with the way the pixel grey value sequence is specified. Two dimensional transforms provide the same information for all radial directions on an image (relative to image center). Fig. 6.1 (Shuchman et al., 1979) is an idealized representation of ocean swell images and their two dimensional Fourier transforms. Power as a function of frequency may be determined by integrating the spectral power density within a given bandwidth filter. In the two

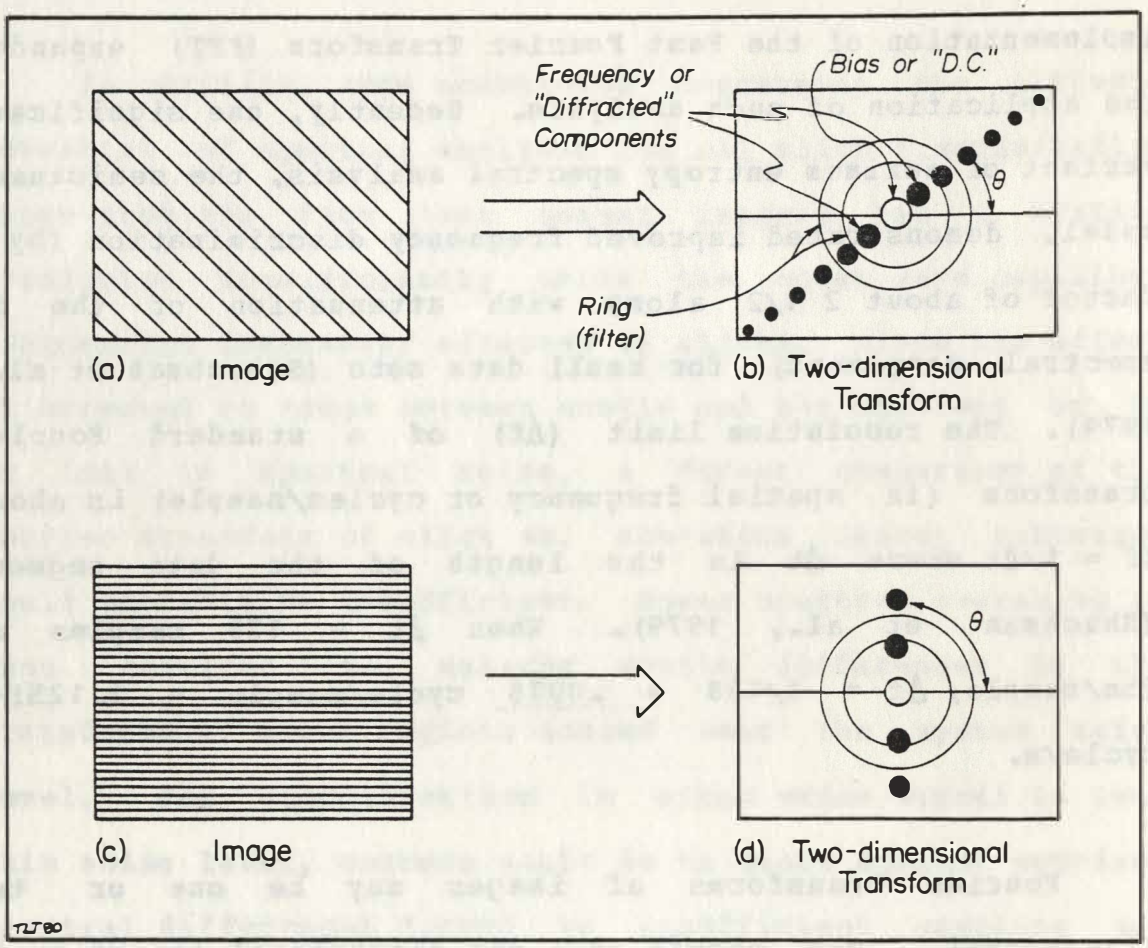

Fig. 6.1 contains diagrams of images with linear features at regular intervals and the Fourier transforms of these images. Note that the distribution of structure in the transform is governed by the frequency and orientation of spatially repetitive pattern in the images. (Shuchman et al., 1979). The ring superimposed on the transforms corresponds to a single example of the eight frequency filters utilized in the power spectrum averaging proceedure described herein.

dimensional transform, an annular (concentric) ring approach can be utilized to accomplish this frequency specific integration. Ringwidth corresponds to bandwidth or integration interval. The larger the ring radius from the transform center (zero frequency) the higher the filtered frequencies. Similarly, the transform may be filtered in azimuth to determine the directional nature of repetitive features in the image by using radially shaped sections or wedges. Wedge and ring filters may be combined to determine power as a function of both frequency and azimuth.

Target or pattern recognition by the determination of characteristic spectral signatures has been pursued with varying degrees of success. Byran, Stromberg and Farr (1977) used azimuthal wedges as narrow as 1° in integrating the amplitude of the Fourier transform to determine the orientation of binary ice lead images. Leachtenauer (1977) used 5° azimuthal wedges and 32 equally divided rings for frequency filtering. His classification analysis of a set of land use categories found that spatial frequency (ring) data was preferred. The directional (wedge) data was not particularly useful.

Lendaris and Stanley (1970) used 9° wedges and 20 annular rings in their analysis of a wide variety of cultural and artificial targets. They noted that the ring

signature for a scan area containing no regular pattern will fall off exponentially as a function of radius, assuming the width of the ring window is such that it cannot resolve the fine frequency characteristics of a narrow scan-aperture. If the scan area does contain a regularly occuring feature, the energy in the spatial frequency power spectrum is redistributed and yields bright spots in certain areas of the the spectrum (transform). The spectral power from the ring window that coincides positionally with bright spots on the transform will be higher that expected from the exponential model. If a ring window reading is equal to or larger than its neighbor on the low frequency side, then the scan area can be assumed to have some kind of feature regularity. For some of their test features (e.g., aircraft) Lendaris and Stanley (1970) used only ring signatures (to effect discrimination) emphasizing that in such an approach the dimensional information (in the spectrum analysis) is independent of the orientation or position of the target/object. They further found a high degree of correlation evident between object dimensions computed from transform signatures and measured directly from images.

In the context of oceanographic application, Beal (1979) confirmed the ability of the Seasat-A SAR to detect longwave swell systems through spectral analysis. Hea

detected and measured a 210m deep-water swell (11.7 sec period) through four successive locations to shallow water in a near-threshold Seasat imaging situation. Prior to taking the transform of a 15 X 15 km area, he performed a 7 X 7 element unweighted running average on the pixels of an equivalent 6 m resolution image. Moore (1979) evaluated the effects of noncoherent averaging of pixels on spatial resolution and found optimum use of a SAR aperture would require a 3 pixel average. Shuchman and others (1978) compared the spectrum of non-Gulf Stream and Gulf Stream images and found that the non-Gulf Stream image transform had fewer high frequency components. They employed a 256 X 256 FFT on X-band, 5 m resolution SAR images. Wave spectrum data evaluated by Hsiao (1978) showed relative azimuthal power distributions on the transform of about a 5:1 maximum / minimum ratio. (Appendix 3 summarizes our determination of a swell wave length via spectral analysis using Seasat SAR image Rev308).

6.3 Analysis Procedure

The rationale for our approach simply considered that the important spectral bands for discrimination were those closest to the spectrum caused by the capillary waves and thus probably most affected by oil slicks. To effect maximal smoothing, wide frequency filters and no azimuthal

wedges were established. It is significant that some of the work previously cited derived only annular ring signatures, because such sampling was independent of orientation of a single object, or the relative orientation and location among a set of similar objects.

The following sequence of spectral power evaluations was employed:

- Calculation of the FFT of 128 X 128 pixel subimages from both oil affected and non-oil affected areas. These areas were defined in section 5.

- Conversion and scaling of spectral power values from the transform into byte (DN = 0 to 255) representative values.

- Multiplication of the scaled spectral power by each of eight registered masks which uniformly divide the normalized spectral frequency scale (which ranges from 0 to .5 cycles/sample).

- Determination of the mean spectral power in each ring (mask).

oaNormalization of the above values using the centrala ring which contains the image bias and lowest frequencya spectral power values.a

oaComparison of the relative mean spectral powers of oila slick vs. non oil slick images.a

6.4 Ring masks (Filters)

Annular masks for spatial frequency filtering used pixel values of DN = 1 within the ring and DN = 0 external to the ring. Registration of the ring and transform 'images' was followed by multiplication of the registered transform and ring pixels to effect filtering. Rings were set up by first generating a circular conical spot image with a linear brightness decrease from image center to the edges. A subsequent image was generated on a DN = 0 background with pixel values of 1 occurring whenever the registered input image pixel values fell within the disired upper and lower grey values defining ring radii. Table 6.1 summarizes the inner and outer radii of the rings, and the total and relative number of pixels per ring. The spatial frequencies and the deep water ocean wavelengths which would give increased spectral power are also shown.

Table 6.1

Ring Frequency Filters

Ring #	Radius Inner	Outer	# Pixels in ring r_i	Relative # pixels	Spatial freq.	Deep water swell wavelength
1	1	8	2882	19.342	.0625 cycle/ sample	400 m
2	9	16	2556	17.154	.125	200
3	17	24	2144	14.389	.1875	133
4	25	32	1776	11.919	.25	100
5	33	40	1346	9.034	.3125	80
6	41	48	944	6.336	.375	67
7	49	56	560	3.758	.4375	57
8	57	64	149	1.000	.5	50

note: based on a 128 x 128 data sample each ring is about 8 frequency resolution cells wide.

6.5 Comparison of the Spectral Power ins Oil Slick and Non Oil Slick SAR Images

The spatial frequency spectral power was determined from the transform of each subimage as subsequently frequency filtered by the series of eight annular rings. For each ring a histogram of power level distribution, as well as its mean and standard deviation, was determined. Because these histograms as initially determined included DN = 0 pixels from both inside and outside the ring, adjustment of the raw power values was necessary. This raw power value adjustment was done in two steps. Since the initially computed spectral power had been linearly stretched (or compressed) to fill the DN range of 0 to 255, the maximum power value ($norm_{max}$) of each subimage which had beens adjusted to 255 was noted. (The minimum power value was always set to 1.0 by the Fourier transform program). Then $norm_{max}/255$ as a multiplier was used to convert the DN range back to the original spectral power values (see Table 6.2). Note that the lowest $norm_{max}$ is for the subimage transform 308DARK, as expected. The highest value is from 308E. There is no significant difference in the $norm_{max}$ values for the oil slick vs. non oil slick subimages in the sets from the same image.

A second multiplier adjusted the mean power of each

Table 6.2

Normalization Values

Oil Slick Images

Image	$norm_{max}$	$norm_{max/255}$
308D	2844.01	11.310
308B	3801.88	14.909
308F	4168.68	16.348
308E	5495.39	21.551
308A	1047.12	4.106
552BB	794.32	3.115
552DD	2884.01	11.310
552AA	602.55	2.363
308C	190.54	.747
552CC	131.82	.517

Non Oil Slick Images

308X	1584.88	6.215
308V	501.18	1.965
308Z	549.53	2.155
308Y	2511.88	9.851
308SW2	549.53	2.155
308DARK	83.17	.326
552YY	630.95	2.474
552ZZ	758.57	2.975
552XX	524.8	2.058
552WW	501.18	1.965

ring appropriately upward by the exclusion (from the mean calculation) of all the DN = 0 pixels occurring outside the ring. This fraction was simply the ratio $16384/r_i$ (termed the mean multiplier). It is given in Table 6.3. The numerator is the total number of pixels in each ring subimage. r_i is the total number of DN = 1 pixels in each ring (see Table 6.1). The adjustment of the mean raw power, mu, to the proper ring mean power, mu' , is simply

$$mu'_i = \frac{mu' \times 16384}{r_i} \times \frac{norm_{max}}{255} .$$

Finally, to compare the two categories of oil slick vs. non oil slick affected backscatter for subimages from Seasat revolution numbers 308 and 552, the relative mean spectral power as a function of ring number was computed. The normalizing power value is mu'_{8e} (where ring 8 is the central, dc and lowest frequency components ring). The relative values are summarized in Table 6.4 in increasing power and plotted in Figs. 6.2 and 6.3 as a function of frequency. Note the greater drops in the oil slick images.

For a reference condition of uniform power density in a transform (eg. as in the transform of an image of Gaussian noise), the relative mean ring power (as a function of

Table 6.3

Mean Power Adjustment

Ring	μmult	relative μmult	109.96/μ mult
1	5.685	.052	19.342
2	6.410	.58	17.154
3	7.642	.069	14.389
4	9.225	.084	11.919
5	12.154	.111	9.047
6	17.356	.158	6.336
7	29.257	.266	3.758
8	109.960	1	1

Table 6.4

Annular Ring Normalized Mean Power

Oil Slick Images

Image Transform	Ring (——> increasing frequency) 7	6	5	4	3	2	1	Σ_{1-7}	Σ_{1-6}
308D	.044	.017	.012	.009	.007	.006	.006	.101	.057
308B	.089	.020	.014	.012	.010	.009	.007	.161	.072
308F	.087	.025	.015	.011	.009	.008	.008	.163	.076
308E	.093	.038	.028	.022	.020	.016	.014	.231	.138
308A	.182	.049	.040	.031	.026	.023	.019	.370	.188
552BB	.163	.075	.070	.054	.048	.043	.039	.492	.329
552DD	.144	.095	.071	.061	.052	.043	.042	.508	.364
552AA	.198	.113	.087	.074	.071	.061	.056	.660	.462
308C	.271	.144	.118	.108	.084	.079	.075	.879	.608
552CC	.440	.312	.300	.245	.210	.187	.161	1.855	1.415

Non-Oil Slick Images

308X	.123	.061	.045	.039	.033	.029	.027	.357	.234
308V	.162	.108	.078	.063	.048	.044	.040	.543	.381
552XX	.223	.159	.138	.110	.106	.089	.080	.905	.682
308Y	.260	.220	.195	.155	.140	.124	.118	1.212	.952
552WW	.355	.233	.217	.194	.165	.153	.142	1.459	1.104
308SW2	.541	.414	.288	.319	.242	.229	.219	2.252	1.711
308DARK	.614	.487	.485	.375	.289	.271	.220	2.543	1.929
552YY	.692	.641	.548	.451	.412	.361	.357	3.462	2.770
552ZZ	.709	.623	.573	.523	.425	.392	.371	3.616	2.907

note: ring 8 = 1.0 for all images; see table 6.2 for normalizing value

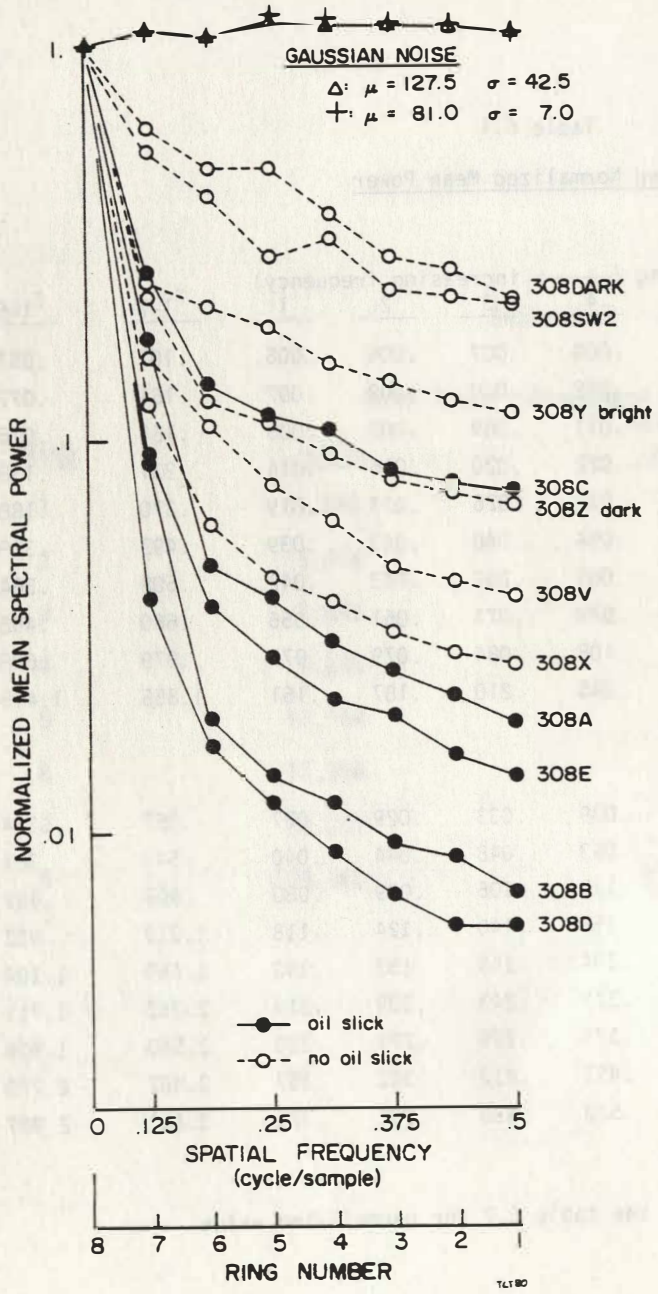

Fig. 6.2 depicts graphically, for Rev 308 oil and non-oil subimages, the drop off in normalized mean spectral power as a function of spatial frequency. Values along the ordinate are determined by averaging power in each of eight circular masks, or rings. The results of similar processing and calculation on two images of Gaussian noise are also plotted. These show no significant drop in normalized power.

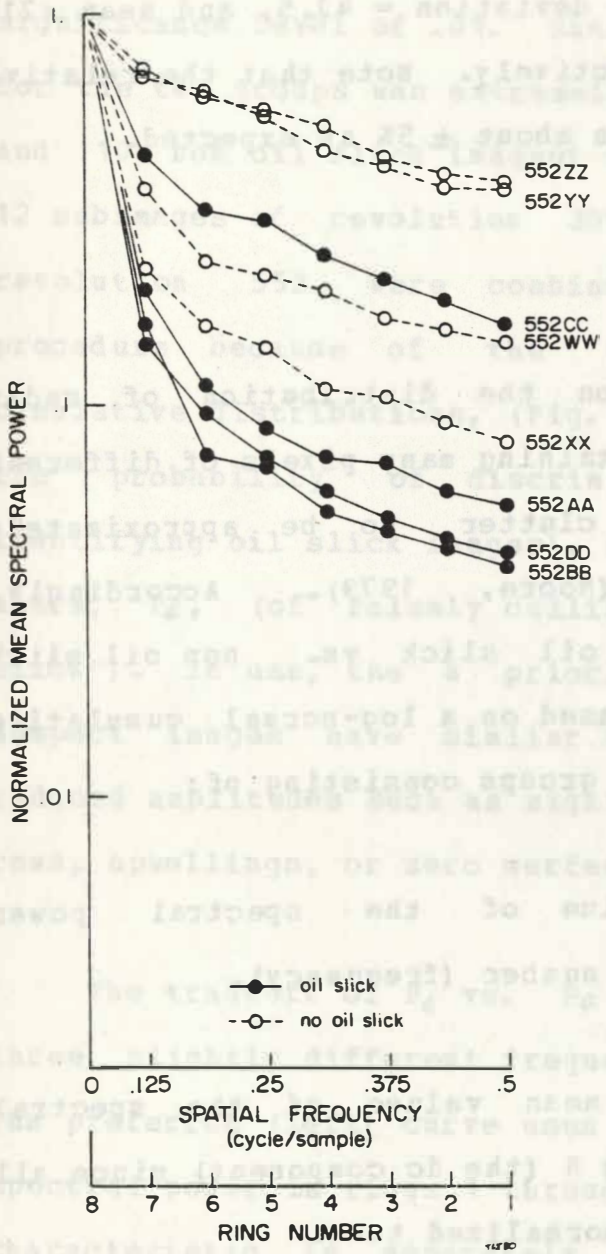

Fig. 6.3 depicts graphically, for Rev 552 oil and non-oil subimages, the drop off in normalized mean spectral power as a function of spatial frequency. Values along the ordinate are determined by averaging power in each of eight circular frequency masks, or rings.

increasing frequency) would remain constant. Figure 6.2 includes two such curves as determined from the transforms of two Gaussian noise images. The image noise parameters were meana= 127.5, standard deviation = 42.5, and mean =21, standard deviationa= 7 respectively. Note that the relative mean power is constant within abouta± 5% as expected.

6.6 Discrimination Criteria

Experimental evidence on the distribution of radar clutter from large areas containing many pixels of different constituents shows the clutter to be approximately log-normally distributed (Moore, 1979). Accordingly, diagnostic comparisons of oil slick vs. non oil slick images have been generated based on a log-normal cumulative probability distribution for groups consisting of:

- oaThe relative mean value of thea spectral power parametric in each ring number (frequency).a

- oaThe sum of the relative mean values of the spectrala power omitting only ring 8 (the dc component) since alla these values have been normalized to 1.a

- oaThe sum of the relative mean values of the spectral power omitting that from rings 7 and 8.

In the last case, the two groups were significantly different as indicated by a small sample t test at a significance level of .01. Since the total data sample size for the two groups was extremely low (10 oil slick images and 10 non oil slick images) the appropriate data from the 12 subimages of revolution 308 and the 8 subimages of revolution 552 were combined. This is a reasonable procedure because of the power normalization. The cumulative distributions, (Fig. 6.4) respectively determine the probability of discrimination, P_d, (of correctly identifying oil slick images), and the probability of false alarm, P_f, (of falsely calling a non oil slick image "oil slick"). In use, the a priori information is that the suspect images have similar spatial patterns of similarly reduced amplitudes such as might be due to oil slicks, wind rows, upwellings, or zero surface stress.

The tradeoff of P_d vs. P_f is shown in fig. 6.5 for three slightly different frequency discrimination criteria. The preferred (left) curve uses the sum of the relative mean spectral power in rings 1 through 6. Essentially the same characteristic is separately displayed by each of the constituent rings (only 1 and 2 are shown). With the inclusion of the low spatial frequencies of ring 7 a somewhat high false alarm rate is experienced. The reason

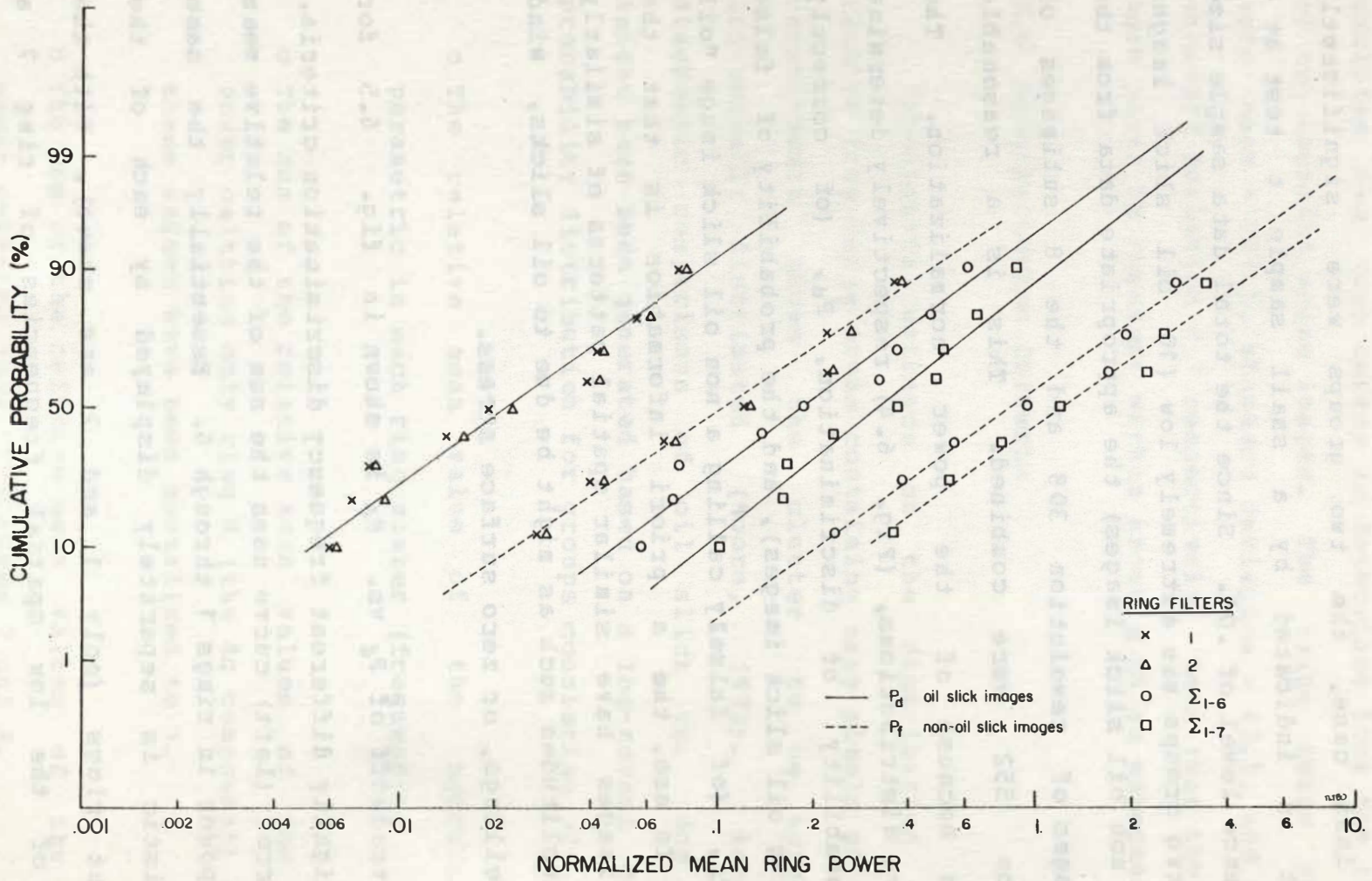

Fig. 6.4 shows cumulative probability of occurrence plots for several potential spectral power discriminants of oil slick vs. non oil slick SAR subimages. Filter combinations compared are listed under Ring Filters.

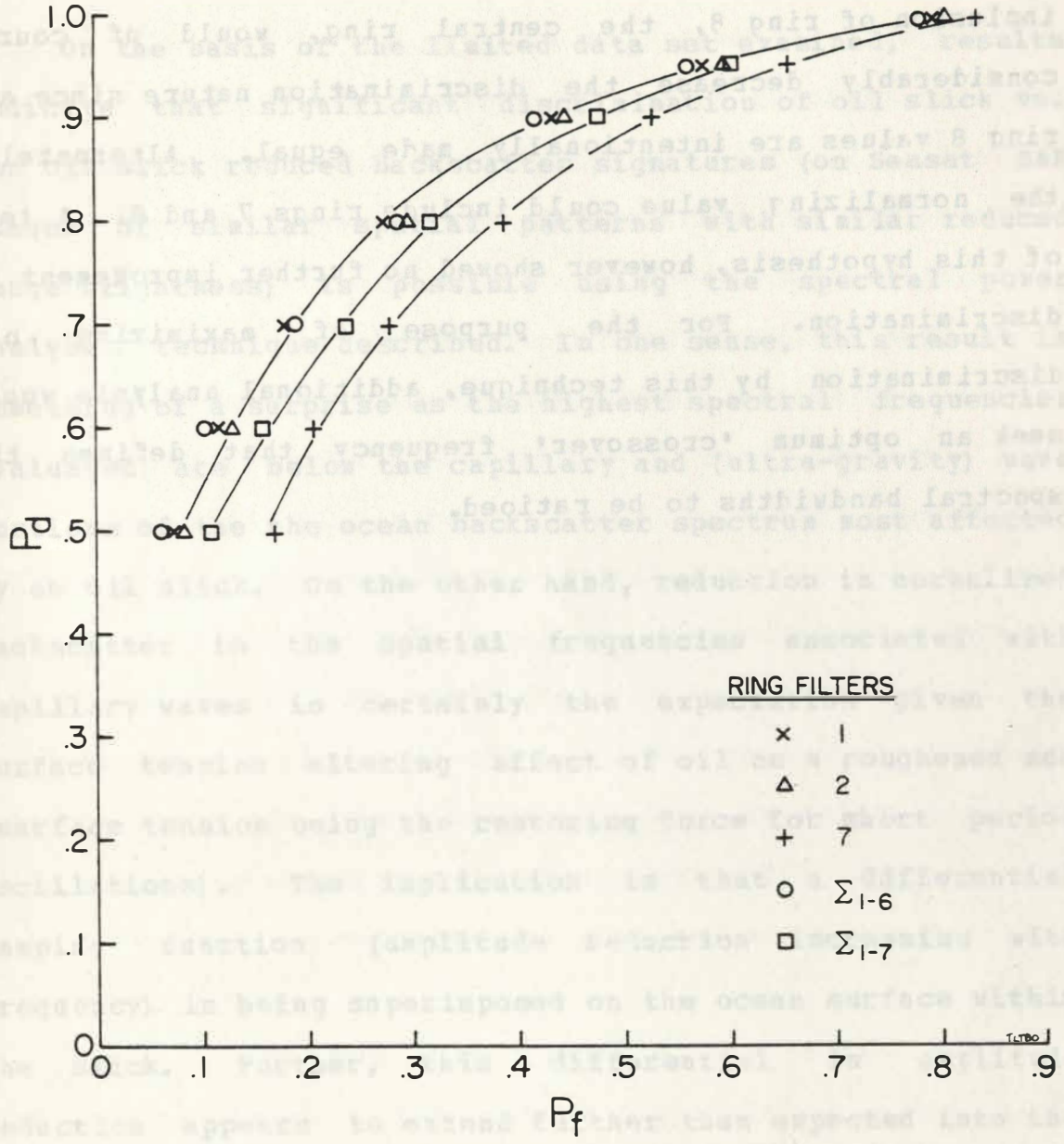

Fig. 6.5 rates several potential spectral power discriminants of oil slick vs. non oil slick SAR subimages using the tradeoff in probability of detection (P_d) vs. the probability of false identification (P_f) as an indicator.

for this is shown in the right-most curve, the poorer discrimination capability of ring 7 alone. The further inclusion of ring 8, the central ring, would of course considerably decrease the discrimination nature since all ring 8 values are intentionally made equal. Alternately, the normalizing value could include rings 7 and 8. A test of this hypothesis, however showed no further improvement in discrimination. For the purpose of maximizing oil discrimination by this technique, additional analysis would seek an optimum 'crossover' frequency that defines the spectral bandwidths to be ratioed.

7.0 Conclusions

On the basis of the limited data set examined, results indicate that significant discrimination of oil slick vs. non oil slick reduced backscatter signatures (on Seasat SAR images of similar spatial patterns with similar reduced image brightness) is possible using the spectral power analysis technique described. In one sense, this result is something of a surprise as the highest spectral frequencies evaluated are below the capillary and (ultra-gravity) wave portions of the the ocean backscatter spectrum most affected by an oil slick. On the other hand, reduction in normalized backscatter in the spatial frequencies associated with capillary waves is certainly the expectation given the surface tension altering affect of oil on a roughened sea (surface tension being the restoring force for short period oscillations). The implication is that a differential damping function (amplitude reduction increasing with frequency) is being superimposed on the ocean surface within the slick. Further, this differential in amplitude reduction appears to extend further than expected into the longer period spatial frequency components of the ocean surface with the result that a more rapid fall off in the normalized (to image bias) backscatter spectrum is observed for oil affected surfaces than for similar appearing non oil influenced surfaces.

The preferred frequency discriminant for making this oil/non-oil determination used the sum of the relative mean spatial frequency powers for the spectral region of about .125 to .5 cycles/sample (.005 to .02 cycles /meter). The discriminant is intentionally insensitive to the effects of image bias and contrast stretching. It is interesting to note that in the process of deriving the cumulative probability of the discriminant values, several subimages of each category were identified as incorrectly spatially positioned due to their inordinately high (and low) discriminant values. Improved confidence in this spatial frequency discriminant requires further data evaluation including investigation into the nature of SAR system (and coherent processor) noise and its threshold characteristics. The integration of this discriminant with the total diverse set of oil slick sensors further suggests that a complete information system analysis is desirable.

The practical mandate to further explore the $\sigma_{slick} / \sigma_{sea}$ relationship for SAR systems arises from today's trend to produce crude oil in inhospitable climates and to transport it in extremely large and unwieldy vessels. Under these circumstances, accidental spills will inevitablyt increase in probability, magnitude, and adverse impact. Provision of accurate spill location and extent information

in timely fashion and independent of inclement weather would prove a significant mitigating countermeasure to these undesirable side effects of energy production. The oil slick discrimination capabilities of Seasat-A SAR suggested by this analysis indicate that such a space borne imaging radar system would be of considerable utility when integrated into a complete oil spill detection operation. Further investigation is therefore suggested in both oil slick signature refinement and real or near real time data processing.

8.0 References Cited

Barger, W., and W. Garret, "Effects of an Artificial Sea Slick upon the Atmosphere and the Ocean," Journal of Applied Meteorology, Vol. 9, pp. 396-400, June, 1970.,

Beal, R., "The Seasat SAR Wind and Ocean Wave Monitoring Capabilities. A Case Study for Pass 1339M," The John Hopkins University, Contract No. JHU/APL SIR 79U-019, 1979.

Blackman, R., and J. Tukey, The Measurement of Power Spectra, Dover Publications, New York, 1958.

Bryan, L., W. Stromberg, and T. Farr, "Computer Processing of SAR L-Band Imagery," Photogrammetric Engineering and Remote Sensing, Vol. 43, pp. 1283-1294, Oct. 1977.

Cox, C. and W. Munk, "Statistics ofe the Sea Surface Derived from Sun Glitter," Journal of Marine Research, Vol. 13, pp. 198-227, 1954.e

Dibblee, T., "Geology of the Santa Ynez Mountains, Santa Barbara County, California," Bulletin 186, California Division of Mines and Geology, San Francisco, 1966.

Elachi, C., and W.E. Brown, "Models of Radar Imaging of the Ocean Surface Waves", IEEE Journal of Oceanic Engineering, Vol.OE-2, No.1, January 1977.

Guinard, N.W., and C.G. Purves, "The Remote Sensing of Oil Slicks by Radar," Navel Research Laboratory, Project No. 71404-A004, U.S. Coast Guard, Washington, D.C., 1970.

Hsiao, V., "The Comparison Between the Synthetic Aperture Radar Imageries and the Surface Truth of Ocean Waves," Oceans 1978, Fourth Annual Combined Conference, Washington, D.C., pp., 385-389, Sept., 1978.

Imray, R., and M Stone, "Characteristics of Sea Clutter at High Frequency," IRE Transactions on Antennas and Propagation, AP-5(1), pp. 164-165, 1957.

Jordan, R., and D. Rodgers, "The Seasat-A Synthetic Aperture Radar Imaging Radar System.", presented at the Western Electronics Conference, Los Angeles, 1976.

Jordan, R., "The Seasat-A Synthetic Aperture Radar Design and Implimentation," presented at NASA Synthetic Aperture Radar Conference, Las Cruces, New Mexico, March, 1978.

Kotlarski, J.B., and H.R. Anderson, "Oil Slick Detection by X-Band Synthetic Aperture Radar", Technicale Report, Hughes Aircraft Company, 1977.

Kraus, S.P., and J.E. Estes, "Oil Seep Survey over Coal Oil Point and the Santa Barbara Channel", Final Report, contract No. LC-6068, prepared for the California State Lands Division, Dec. 1976.

Kraus, S.P., J.E. Estes, and R.e Vollmers, "Comparativee Evaluation of Real and Synthetic Aperature Radars for the Detection of Oil Pollution in the Santa Barbaea Channel", Proceedings of the 1977 Oil Spill Conference, Vol.1, 1977, pp. 203-208.

Krishen, K., "Detection of Oilspills Using a 13.1 GHz Radar Scatterometer," Proceedings of the Eighth International Symposium on Remote Sensing of Environment, ERIM, pp. 1105-1111, 1972

Lange, P., and Huhnerfuss, H., "Drift Resopnse of Monomolecular Slicks to Wave and Wind Action," Journal of Physical Oceanography, Vol. 8e pp. 142-150, 1978.

Leachtenauer, J., "Optical Power Spectrum Analysis: Scale and Resolution Effects," Photogrammetric Engineering and Remote Sensing, Vol. 43, pp. 1117-1125, Sept. 1977.

Lendaris, G., and G.e Stanley, "Diffraction-Pattern Sampling for Automatic Pattern Recognition," Proc. IEEE, Vol. 58, pp. 198-216, Feb., 1970.

Long, M.W., Radar Reflectivity of Land and Sea, Lexington Books, D.C., Heath and Co., Lexington, Ma, 1975.

Mauer, A., and A.T. Edgerton, "Flight Evaluation of U.S.e Coast Guard Airborne Oil Surveillance System," Proceedings of the Conference on Prevention and Control of Oil Spills, San Francisco, American Petroleum Institute, March 1975.

Mitsuyasu, H., "Measurement of the High-Frequency Spectrum of Ocean Surface Waves," Journal of Physical Oceanography, Vol. 7, pp. 882-889, 1977.e

Moore, R., "Tradeoff Between Picture Element Dimensions and Noncoherent Averaging in Side-Looking Airborne Radar," IEEE Transactions on Aerospace and Electronic Systems, Vol. AES-15, no. 5, pp. 697-708, Sept., 1979.

Moore, R.K., and A.K. Fung, "Radar Determination of Winds at Sea," Proceedings of the IEEE, Vol. 67, No. 11, November, 1979.

Neu, H.A., "The Hydrodynamics of Chedabucto Bay and Its Influence on the 'Arrow' Oil Disaster", AOI Report, pp. 1976, 1970.

Otnes, R., and L. Enochson, Applied Time Series Analysis, Vol. 1, Basic Techniques, Wiley-Interscience, 1978.

Pierson, W., and R. Stacy, "The Elevation, Slope, and Curvature Spectra of Wind Roughened Sea Surfaces," NASA Contractor Report CR-2247, 1973.

Pilon, R. and C. Purves, "Radar Imagery of Oil Slicks," IEEE Transactions on Aerospace and Electronic Systems, Vol. AES-9, No. 5, 1972.

Raney, R.K., and Lowry, R.T., "Ocean WaveoImagery and Wave Spectra Distortions by Synthetic Aperture Radar", Proceedings of the 12th Inter. Sym. on Remote Sensing of Environment, ERIM, pp. 683-702, 1978.o

Reitz, M., United States Geological Survey, Oil Production Monitering Group, Ventura, California, quoted in the Santa Barbara News Press, July, 30, 1980.

Sabins, F., Remote Sensing Principles and Interpretation, W.H. Freeman and Co., San Francisco, 1978.

Samuels, W., and K. Lanfear, "An Oilspill Risk Analysis for the Central and Northern California (proposed sale 53) Outer Continental Shelf Lease Area," U. S. Geological Survey Open-File Report 80-211, 1980.

Schwartzberg, H.G., "The Movement of Oil Spills", Proceedings of the Joint Conference on Prevention and Control of Oil Spills, June 1971, pp. 489-494.

Shuchman, R.A., E.S. Kasischke, and A. Klooster, "Synthetic Aperture Radar Ocean Wave Studies", Final Report to NOAA on contract 7-35328, ERIM, September 1978.

Shuchman, R., E. Kasischke, A. Klooster, and P.o Jackson, "Seasat SAR Coastal Ocean Wave Analysis," Contract No.o MD-A01-78-00-4339, ERIM, Nov, 1979.

Skolnik, M.I., Radar Handbook, McGraw-Hill Inc., New York, 1970, pp. 1-4.

vanKuilenburg, J., "Radar Observations of Controlled Oilspills," Proceedings of the 10th International Symposium on Remote Sensing of Environment, ERIM, Vol. 1. p. 243-250, 1975.

Vedder, J., H. Wagner, and J. Schoellhamer, "Geologic Framework of the Santa Barbara Channel Region," U. S. Geological Survey Professional Paper 679, Washington, D.C.,o 1969.

Waldman, G.A., R.A. Johnson, and P.C. Smith, "The Spreading and Transport of Oil Slicks in the Open Ocean in the Presence of Wind, Waves, and Currents", Final Report, Contract No. CG-D-17-73, prepared for U.S. Coast Guard, July 1973.

Weissman, D.E., and T.W. Thompson, "Detection and Interpretation of Ocean Roughness Variation Across the Gulf Stream Inferred from Radar Cross Section Observations", IEEE MTS, Oceans 1977, pp. 14B-1,10.

Wilson, R., P. Monaghan, A. Osanik, L. Price, and M. Rogers, "Natural Marine Oil Seepage," Science, Vol. 184(5), pp. 857-865, 1974.

Wilson, M., P. O'Neill, and J. Estes, "Satellite Detection of Oil on the Marine Surface," Fifth Annual Pecora Symposium, Sioux Falls, South Dakota, in press, 1979.

Wilson, M., "Oil Trajectory Modeling in the Coal Oid Point Area of the Santa Barbara Channel," unpublished Master's Thesis, Dept. of Geography, University of California, Santa Barbara, 1980.

Wright, J., "A new Model for Sea Clutter," IEEE Transactions on Antennas and Propagation, Vol. AP-16, 1968.

Wu, C., "A Digital Fast Correlation Approach to Produce Imagery from SAR Data," presented at IEEE, 1980, International Radar Conference, Arlington, Virginia, April 28, 1980.

Appendix 1

Significant variance away from a single monthly average current velocity vector is observed at the Coal Oil Point study area. This variance can be logically partitioned into a turbulent component which can be regarded as random fluctuation, and a cyclical component which is controlled by sub-monthly variation in current driving forces. The first source of variance is illusive and cannot be quantitatively described given the limitations of input data. The second, however, can be partially accounted for.

Of all current driving forces, only tidal ebb and flow can be quantified adequately on an ex post facto basis. This fact has been used to here test the assumption that a certain portion of observed variation around a mean current velocity in the study area is directly related to tidal flux. In an attempt to measure this relatedness a regression analysis has been performed comparing observed current drift velocities with the phase of the tidal cycle. Individual surface drift observations are listed in table 9.1 along with pertinent meteorological information. (Note, all drift data is in degrees true and magnitudes are in knots. Direction is uniformly that towards which flow is moving.) The following notes serve to qualify the

Table 9.1

OBSERVED WIND AND SURFACE DRIFT AT COAL OIL POINT ; 1979-1980

DATE	OBSERVED DRIFT	WIND DRIFT *1	CORRECTED DRIFT *2	MODIFIED BACKGROUND DRIFT FROM BLM DATA	TIDAL DERIVATIVE	TIME (PST) / TIDE CYCLE
MAR. 6, '79	305° ; .28	0 *3	305° ; .28	278° ; .19	0 *4	1100 / SLACK LOW
MAR. 7, '79	37° ; .22	274° ; .14	58° ; .32	278° ; .19	1.1	1500 / INCOMING
AUG. 31, '79	330° ; .50	239° ; .14	346° ; .52	331° ; .19	0	1100 / SLACK LOW
SEPT. 7, '79	287° ; .87	99° ; .14	286° ; 1.0	278° ; .29	2.1	1000 / INCOMING
SEPT. 25, '79	295° ; .43	0	295° ; .43	278° ; .29	0	1200 / SLACK HIGH
SEPT. 28, '79	138° ; .37	130° ; .52	*5	278° ; .29	0	1600 / SLACK HIGH
JULY 8, '80	305° ; *6	0	305° ;	313° ; .29	0	0900 / SLACK
JULY 15, '80	290° ; .47	135° ; .14	296° ; .60	313° ; .29	.75	1200 / INCOMING

Note: all drift data is indicated by direction (degrees true), and magnitude (knots).

Table 9.1

(continued)

OBSERVED WIND AND SURFACE DRIFT AT COAL OIL POINT ; 1979-1980

DATE	OBSERVED DRIFT	WIND DRIFT *1	CORRECTED DRIFT *2	MODIFIED BACKGROUND DRIFT FROM BLM DATA	TIDAL DERIVATIVE	TIME (PST) / TIDE CYCLE
JULY 18, '80	295° ; .35	0	295° ; .35	313° ; .29	.21	1500 / NEAR SLACK
JULY 25, '80	335° ; .62	0	335° ; .62	313° ; .29	1.20	1100 / INCOMING
JULY 29, '80	355° ; .44	0	10° ; .44	313° ; .29	.16	1200 / NEAR SLACK
AUG. 1, '80	20° ; .51	90° ; .21	356° ; .482	331° ; .19	.27	1400 / NEAR SLACK
AUG. 4, '80	310° ; .65	0	310° ; .65	331° ; .19	-.41	0900 / OUTGOING
AUG. 12, '80	340° ; .70	285° ; .14	350° ; .63	331° ; .19	1.0	0900 / INCOMING
AUG. 15, '80	110° ; .30	100° ; .42	*5	331° ; .19	-.30	1600 / OUTGOING
AUG. 22, '80	318° ; .33	0	318° ; .33	331° ; .19	-.43	1200 / OUTGOING
AUG. 25, '80	352° ; .54	114° ; .17	339° ; .646	331° ; .19	-.86	1400 / OUTGOING
AUG. 29, '80	347° ; .77	0	347° ; .77	331° ; .19	1.19	1000 / INCOMING

OBSERVED DRIFT, WIND DRIFT, CORRECTED DRIFT, AND MODIFIED BACKGROUND DRIFT FROM BLM DATA ARE INDICATED BY DIRECTION (DEGREES TRUE) ; MAGNITUDE (KNOTS).

BCL 9/80

acquisition and interpretation of this drift data. They are referæd to in table 9.1.

*1 Wind drifta = direction towards which wind is blowinga plus 20° for Corriolis acceleration, and adjusted in magnitude by a factor of 0.037 as per chapter 4 discussion.

*2 Corræcted drifta= observed drift minus wind drift. This yieadds drift attributable to background flow plus tidal forcing.

*3 When recorded winds dropa below 4 knots, no wind drift affect is calculated.

*4 Tidal derivatives less than .1 are set to zero.a

*5 In actuality, wind drift is a function of the squarea of wind speed. As such, for winds over 10 knots, wind drift begins to dominate flow (see Sept 28, 1979 and Aug 15, 1980 in table 9.1). The empirical constant 0.037 is only adequate for a narrow range of wind speeds. Since this exercise seeks to establish forcing parameters other than wind, days on which winds exceed this range are dropped from the curve fitting procedure.

*6 On some days no current speed measurements coulda be obtained.

Subject to these assumptions and qualifications, this drift data was then run through a regression test which compared corrected drift (minus wind associated drift) with the absolute value of the tidal curve derivative (determined by sampling a curve splein fit through daily tidal highs and lows. The absolute value of the derivative was incorporated, as both large negative and large positive values imply significant tidal flux, whereas derivatives near zero denote temporary minimums of kinetic energy.

The results of comparing both current direction and current magnitude with the tidal derivative appear in tables 9.2 and 9.3 respectively. In the case of direction, essentially no correlation is observed. Current magnitude, however, shows a significant level of correlation (R = .75) with the absolute value of the tidal derivative. A plot of the scatter diagram and regression line appears in fig 9.1.

Table 9.2

LINEAR REGRESSION OF CURRENT DIRECTION
AT COAL OIL POINT
ON TIDAL DERIVATIVE

Basic Descriptive Statistics

	Mean	Standard Deviationi	Correlation
Tidal Derivative	0.32	0.83	
			0.20i
Current Direction	331.	35.53	

Model Paramater Influences

	Point Estimate	Standard Error	Lower Confidence Limit	Upper Confidence Limit
Regression Coefficient	8.67	11.56i	-16.i	33.i64i
Intercept	328.	10.02i	307.	350.i

Analysis of Variance

Source of Variation	Degrees of Freedom	Sums of Squares	Mean Squares	F-Value	Prob (Exceeding F Under H_)
Regression	1.00	732.	732.i	0.56i	0.47i
Residual	13.00	16943.	1303.i		
Total	14.00	17676.			

Table 9.3

LINEAR REGRESSION OF CURRENT VELOCITY
AT COAL OIL POINT
ON ABSOLUTE VALUE OF TIDAL DERIVATIVE

Basic Descriptive Statistics

	Mean	Standard Deviation	Correlation
Tidal Derivative	0.65	0.60	0.75
Current Magnitude	0.54	0.19	

Model Paramater Influences

	Point Estimate	Standard Error	Lower Confidence Limit	Upper Confidence Limit
Regression Coefficient	0.24	0.06	0.12	0.37
Intercept	0.38	0.05	0.27	0.49

Analysis of Variance

Source of Variation	Degrees of Freedom	Sums of Squares	Mean Squares	F-Value	Prob (Exceeding F Under H)
Regression	1.00	0.30	0.30	16.36	0.00
Residual	13.00	0.23	0.02		
Total	14.00	0.53			

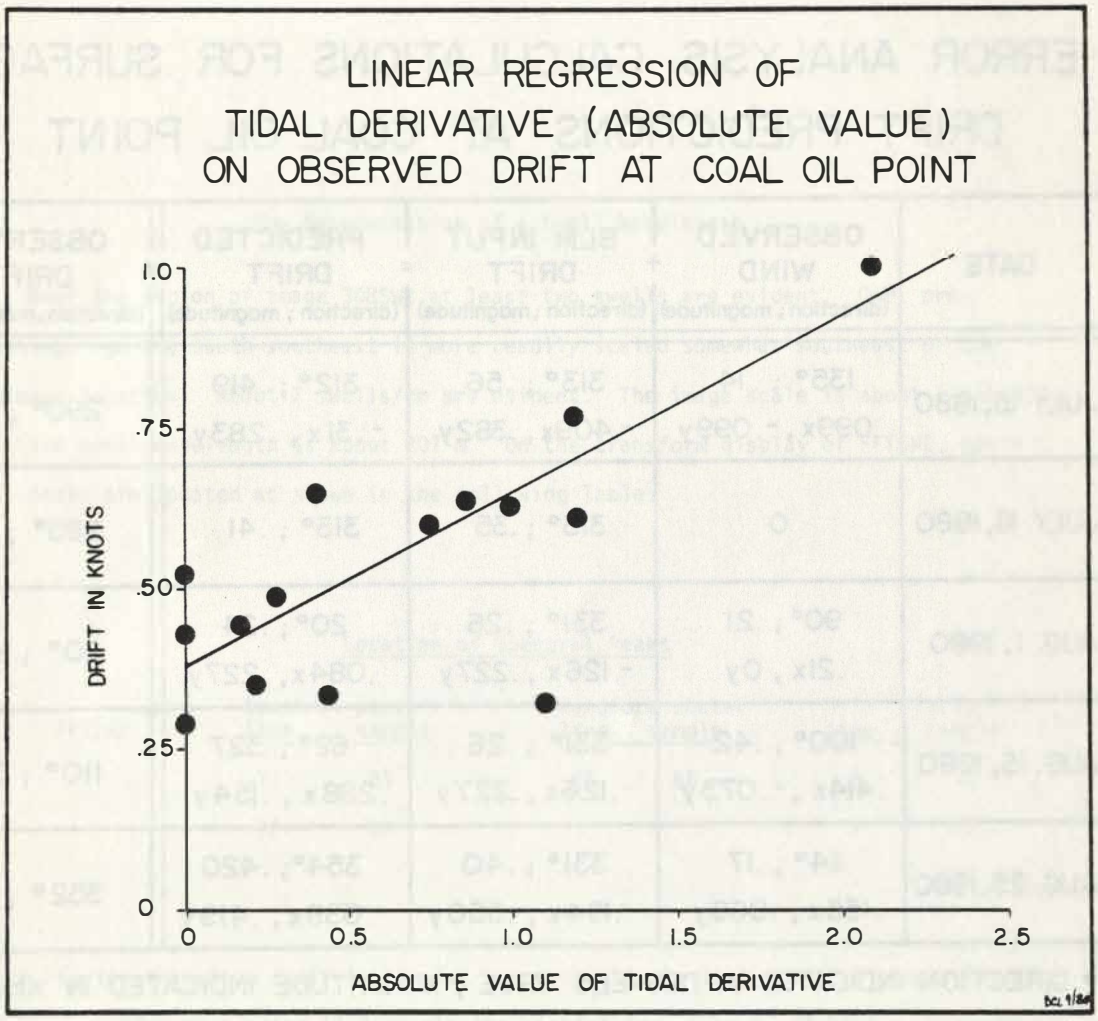

Fig 9.1 linear regression plot

Appendix 2

ERROR ANALYSIS CALCULATIONS FOR SURFACE DRIFT PREDICTIONS AT COAL OIL POINT

DATE	OBSERVED WIND * (direction ; magnitude)	+	BLM INPUT DRIFT (direction ; magnitude)	=	PREDICTED DRIFT (direction ; magnitude)	vs	OBSERVED DRIFT (direction ; magnitude)
JULY 15, 1980	135° ; .14 .099x , -.099y		313° ; .56 -.409x , .382y		312° ; .419 -.31x , .283y		290° ; .47
JULY 18, 1980	0		313° ; .35		313° ; .41		295° ; .35
AUG. 1, 1980	90° ; .21 .21x , 0y		331° ; .26 -.126x , .227y		20° ; .24 .084x, .227y		20° ; .51
AUG. 15, 1980	100° ; .42 .414x , -.073y		331° ; .26 -.126x , .227y		62° ; .327 .288x , .154y		110° ; .30
AUG. 25, 1980	114° ; .17 .155x , .069y		331° ; .40 -.194x , .350y		354°; .420 -.039x , .419y		352° ; .54

* DIRECTION INDICATED IN DEGREES TRUE ; MAGNITUDE INDICATED IN KNOTS

In conducting error analysis, five predictions of surface drift for a point in the study area were generated using all the driving assumptions outlined in chapter 4. Wind was observed at the site, while current and tidal influences were input as described. At the same time, actual surface drift measurements were taken using a Teledyne Gurley cable suspended current meter. The results of these comparative exercises appear below.

Appendix 3

The Determination of a Swell Wavelength

Near the region of image 308SW2 at least two swells are evident. One, propagating from the south-southeast is more readily scaled somewhat southeast of the subimage location. About 7 swells/cm are evident. The image scale is about 1:145,000, thus the swell wavelength is about 207 m. On the transform display of FFTSW2, spectral peaks are located as shown in the following Table.

Location of Spectral Peaks

FFTSW2	Spectral peaks line	sample	Transform center line	sample	Δ pixels line	sample
	71	81	65	66	6	15
	72	83			7	17

These Fourier transform radii (Δ pixels) are respectively 16.2 and 18.4 pixels from the center. For an average 17.3 pixels the spatial frequency is 17.3/64 x .5 cycles/sample or .135 cycles/sample. Thus the swell wavelength is 25 m/.135 or 185 m (@ 112° from image vertical).